Demonstrating Aeolus capability to observe wind-cloud interactions

~~Wind-cloud interactions observed with Aeolus spaceborne Doppler Wind Lidar~~

Zacharie Titus[1], Marine Bonazzola[1], Hélène Chepfer[1], Artem G. Feofilov[1], Marie-Laure Roussel[1], Benjamin Witschas[2], Sophie Bastin[3]

[1]Laboratoire de Météorologie Dynamique/Institut Pierre Simon Laplace (IPSL), Sorbonne Université, CNRS, Institut Polytechnique de Paris, Paris, France

[2]Deutsches Zentrum für Luft- und Raumfahrt e.V. (DLR), Institut für Physik der Atmosphäre, 82234 Oberpfaffenhofen, Germany

[3]Laboratoire ATmosphere Milieux Observations Spatiales/Institut Pierre Simon Laplace (IPSL), UVSQ Université Paris-Saclay, Sorbonne Université, CNRS, CNES, Guyancourt, France

Correspondence to: Zacharie Titus (zacharie.titus@lmd.ipsl.fr)

Abstract. Model based studies have shown interactions between wind vertical profiles and cloudiness, but few observational studies corroborate them. The unique observations of Aeolus spaceborne Doppler wind lidar can contribute to fill this gap. In this paper, we merged global Aeolus observations of cloud profiles at full horizontal resolution (3 km along orbit track) with co-located profiles of horizontal winds.

We first observed wind-cloud interactions at regional scale over the Indian Ocean. Aeolus captures the strengthening of the Tropical Easterly Jet in early June 2020, with wind speeds exceeding 40 ms^{-1} in its core, and a simultaneous increase of high cloud fraction up to above 30 %, until the decay of the jet during fall.

Secondly, we observed wind-cloud interactions at cloud scale (between 3-100 km) in different regions. Over the Indian Ocean as well as over cumulus and stratocumulus dominated regions, we found that the wind shear inside clouds is ~~in cloudy sky is always~~ smaller than the wind shear in the clear sky surrounding the clouds~~cloud~~ (statistically significant). In addition, we found that the wind speed difference between the cloud and its surrounding clear sky increases with the clear sky wind shear, especially in cumulus (R=-0.94~~0.93~~) and stratocumulus (R=-0.87~~0.89~~) dominated regions. This study demonstrated that despite its coarse resolution, Aeolus can capture wind perturbations induced by convective motion~~momentum transport~~.

1 Introduction

Clouds play a critical role in Earth's climate as a major component of the water vapor cycle and because they have a large impact on the radiative budget at the top of the atmosphere and at the Earth surface. The formation and development of clouds are controlled by the surface temperature and by the thermodynamic structure of the lower troposphere, but also by dynamic variables. It was shown that fast horizontal winds are responsible for an increased cirrus cloud cover through different mechanisms like advection of humidity from warmer to cooler regions, favoring the in-situ formation of cirrus clouds (Das et al., 2011). Deep convective cloud systems tend to form in regions of large-scale wind convergence. They organize into rain bands and squall lines by the wind shear (e.g., Thorpe et al., 1982 ; Rotunno et al., 1988 ; Parker, 1996 ; Hildebrand, 1998 ; Robe and Emanuel, 2001 ; Weisman and Rotunno, 2004 ; Abramian et al., 2022). The wind shear can also inhibit deep and shallow convection by "blowing off" cloud tops (e.g., Koren et al., 2010 ; Sathiyamoorthy et al., 2004), or increase the cloud cover by tilting cloud tops away from their base (Mieslinger et al., 2019), thus influencing cloud-top height and cloud cover (Helfer et al. 2020). Over marine boundary layers, the wind shear can even locally deplete stratocumulus cloud tops (Wang et al. 2008 ; Schulz and Mellado, 2018). Reversely, clouds can have an influence on winds through their radiative effect. Fujiwara et al. (2004)2004 showed that the radiative cooling associated to anvils creates a temperature gradient at the top of high convective clouds, that can generate a thermal wind. At a large scale, it was shown that the cloud radiative effect impacts the intensity and location of the jet stream by altering temperature gradients and redistributing energy within the atmosphere (Voigt et al, 2021).

To better understand wind-cloud interactions, a large number of studies have been performed. These studies are based on models or meteorological analyses. Observations of winds within cloudy systems are usually performed by radiosondes, airborne or ground based Doppler Radars, and are therefore limited in space and time. In this study, we benefit from the unique capabilities of the Atmospheric LAser Doppler INstrument (ALADIN), a 355 nm spaceborne Doppler Wind Lidar with High Spectral Resolution (HSRL) capabilities onboard the Aeolus satellite (Stoffelen et al., 2005 ; Reitebuch et al., 2012). Aeolus is primarily designed to retrieve profiles of horizontal winds but can also retrieve profiles of clouds (Flamant et al., 2008 ; Dabas et al., 2022 ; Feofilov et al., 2022). During its 5 years of operation, (Aeolus DISC, 2024), Aeolus scanned over a billion kilometers of atmosphere around the globe (Aeolus DISC, 2024), encountering all kinds of cloudy systems at various latitudes. Aeolus thus offers for the first time the possibility to analyze, at global-scale, co-located instantaneous profiles of clouds and profiles of horizontal winds within clouds and their clear sky surroundings.

In its current state, studying wind-cloud interactions with Aeolus is challenging for two reasons. First of all, clouds can be as little as a few tens of meters horizontally (Koren et al., 2008), cloud detection thus needs to be performed at the highest

possible spatial resolution in order to avoid mixing clear and cloudy scenes. Recent work showed that it is possible to perform cloud detection at full horizontal resolution of 3 km (Donovan et al., 2024b ; Wang et al., 2024). Moreover~~We thus developed a cloud detection similar to theirs at 3 km of resolution along the orbit track using Aeolus Level 1A (L1A) data which contains the uncalibrated backscatter signal. Compared to the approach introduced by Donovan et al., 2024b, we apply slight differences such as a compensation of the missing cross-polar signal of Aeolus from a climatology of the GCM-Oriented Cloud-Aerosol Lidar and Infrared Pathfinder Satellite Observation Cloud Product (CALIPSO-GOCCP) observations, as well as the systematic discarding of hot pixels. Secondly~~, the wind profiles are available in a different Aeolus product with a different along-track resolution, therefore an additional processing is necessary to merge clouds and winds.

Aeolus is primarily designed to retrieve vertical profiles of horizontal winds in the troposphere and the lower stratosphere at global-scale. The laser is pointed 35° off-nadir and perpendicular to the satellite track, away from the Sun. The obtained measurement is not the actual horizontal wind $\overrightarrow{U(z)} = \overrightarrow{u(z)} + \overrightarrow{v(z)}$, but the horizontal projection of the wind retrieved along Aeolus Line-of-Sight (LOS, ~~its projection on the laser pointing direction~~ $U_{proj}(z) = \left|\overrightarrow{U(z)}\right|.\cos(\varphi)$ ~~where *u* and *v* are the zonal and meridional winds wind and *φ* the angle between the actual horizontal wind direction and the laser pointing direction~~ (Fig. 1). In most of the Aeolus literature, this wind is noted v_{HLOS}~~, also called the line-of-sight (LOS) in Aeolus literature~~. Hereafter, we use the wind profiles from Aeolus Level 2B (L2B, Baseline 16) scientific wind product. These ~~which have been continuously validated during the mission with airborne lidars (Lux et al., 2020 ; Witschas et al., 2020 ; Witschas et al., 2022), ground based lidars, radars and radiosondes (Ratynski et al., 2023 ; Iwai et al., 2021 ; Belova et al., 2021 ; Baars et al., 2020). Aeolus~~ wind profiles come from two channels. A "Mie channel" retrieves wind within entire optically thin clouds, which cover typically 35 % of the globe on average (Guzman et al., 2017) but also within the upper layers of opaque clouds, which cover typically 31 % of the globe on average. The "Rayleigh channel" retrieves wind in clear sky, which covers the remaining 34 % of the globe on average. ~~The Rayleigh and Mie channels have horizontal and vertical resolutions that vary to optimize the signal to noise ratio and vertical coverage. The latest validation campaigns of Aeolus showed that the systematic error (bias) for wind measurements remained within the mission requirements of 0.7 ms⁻¹ for both Mie and Rayleigh channels, while the random error was about 3 ms⁻¹ for the Mie channel and 5 to 7 ms⁻¹ for the Rayleigh channel.~~ In order to fully benefit from Aeolus observations to better understand wind cloud interactions, it is necessary to resample the Aeolus ~~use statistical approaches with a large number of independent~~ wind profiles at the same fixed resolution as the cloud profiles~~in order to reduce the impact of the random error (reduced by a factor N^1/2 with N independent profiles)~~.

The purpose of this paper is to evaluate the feasibility of studying wind-cloud interactions from large scale to cloud scale (between 3-100 km), making use of our dataset of merged global Aeolus observations of cloud profiles at full horizontal resolution (3 km along orbit track) with co-located profiles of horizontal winds. At a large scale, we particularly focus on the relationship between high cloud cover and the Tropical Easterly Jet (TEJ) over India. At a lower scale, we evaluate the benefit of our observations for the validation of the K-theory for the wind Convective Momentum Transport (CMT).
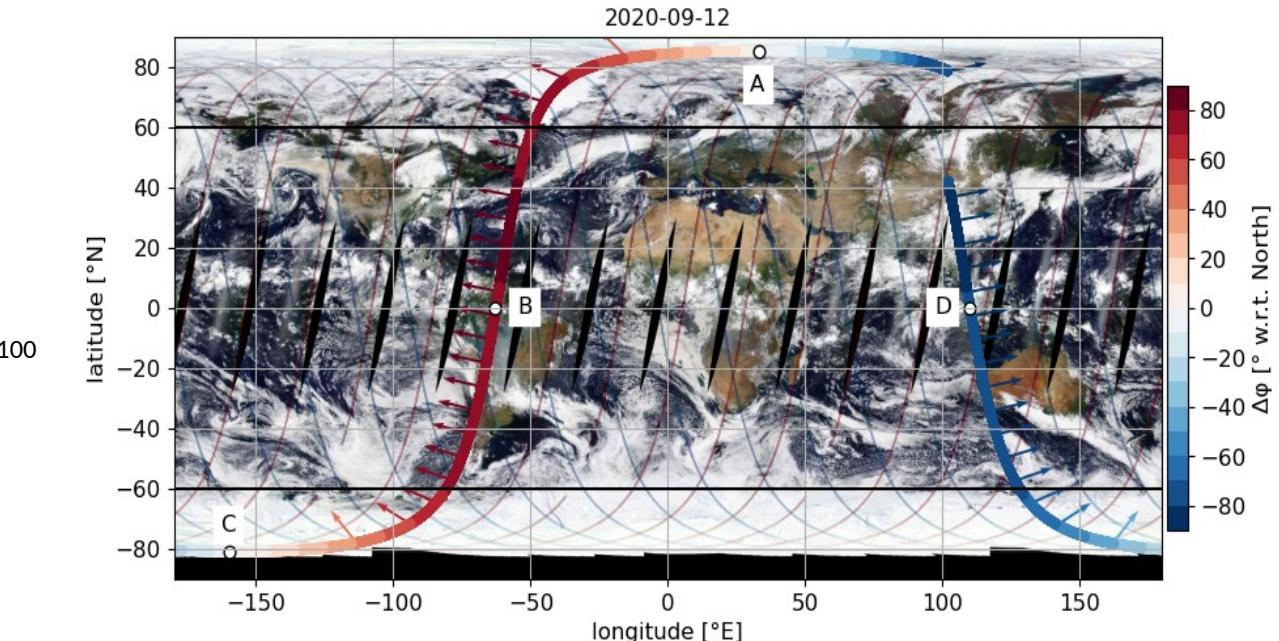
Figure 1: Track of one Aeolus orbit (2020-09-12T09 – 2020-09-12T11). Aeolus retrieves the projection of wind aligned with the arrows. Δφ represents the angle between the South-North axis and the laser pointing direction, counter-clockwise. Thinner curves represent all obits for the day of 2020-09-12. A is the North-most point. B is the equatorial crossing point during descending phase (0600 LT). C is the South-most point. D is the equatorial crossing point during ascending phase (1800 LT)

Section 2 of the paper details the method used to retrieve profiles of clouds. In Sect. 2.2 we assess the quality of this cloud detection by comparing it to another cloud climatology obtained with CALIPSO-GOCCP. In Sect. 3, we re-sample Aeolus L2B Mie and Rayleigh wind observations at 3 km of resolution along track and 480 m 480m vertically and merge them using the cloud mask. We also quantify how much of the natural "sub-grid" variability is missed when re-sampling the wind from 87 km to a higher horizontal sub-grid resolution of 8 km using high spatial resolution airborne Doppler Wind Lidar (DWL) data during AVATAR-T (Aeolus Validation Through Airborne Lidars in the Tropics) campaign, and, and also to a sub-grid resolution of 3 km using a high spatial resolution simulation performed with the Weather Research and Forecasting (WRF) model. Finally, in Sect. 4, we present the first descriptive results that we obtain with this dataset, focusing on

different horizontal scales. We study the Tropical Easterly Jet and its correlation with high cloud fractions. We also assess the difference between cloudy and clear sky winds at cloud scales inferior to 100 km. We conclude this paper in Sect. 5.

120

125

130

135

140

145

2 Processing Aeolus clouds

2.1 Building cloud diagnostics from Aeolus ~~from~~ particulate and molecular backscatter profiles

~~We use the highest resolution Aeolus dataset (L1A), which corresponds to an on-board averaging of 16 subsequent accumulated backscatter profiles resulting in a horizontal resolution of 3 km along orbit track. To estimate the cloud mask, we process Aeolus L1A raw data at the detector level.~~

Hereafter, we build Aeolus cloud statistics based on a cloud mask defined at 480 m vertical resolution and best possible horizontal resolution, to compare Aeolus data with CALIPSO-GOCCP (Chepfer et al., 2010) and to facilitate future use of Aeolus data~~Even though the molecular and particulate channels of ALADIN were designed to detect the radiance backscattered from molecules and particles, respectively, this separation is not perfect. We only use the radiance retrieved~~ by the climate model community through the COSP Lidar Simulator (Bodas-Salcedo et al., 2011). To build this cloud mask from Aeolus particulate and molecular backscatter profiles, we follow ~~detector of the Mie channel. Following~~ an approach similar to the one proposed by ~~that of~~ Donovan et al., 2024b, with the following additions: a cross-polar correction from CALIPSO-GOCCP and a dedicated processing of hot pixels. In this approach, ~~(2024b),~~ we use Aeolus Level 1A (L1A) raw data, with a horizontal resolution of 3 km. We only use the radiance retrieved by the detector of Aeolus Mie channel~~the spectral leak of molecular backscatter and particulate backscatter~~. The spectrum of the radiance illuminating~~reaching~~ the 16 pixels of the detector ~~of the Mie channel~~ consists of a superposition of a narrow peak related to a particulate backscatter and a several times broader peak associated with molecular backscatter (Fig. A1). The position of the centre~~center~~ of the joint envelope represents the direction and the strength of the wind, whereas the integral of the signal is proportional to a total attenuated backscatter.~~, and the ratio between the core and the wings of the envelope is related to particulate-vs-molecular backscatter ratio.~~

For a given profile, we process the spectrum measured by the detector of the Mie channel at each altitude level in six successive steps.

1~~a~~) Discard "hot pixels".

It has been known since the early days of the Aeolus mission that certain pixels of the detector are damaged by cosmic particles and that the number of these pixels almost linearly increases over the mission's lifetime (Weiler et al., 2021). We discard the hot pixels following the hot pixel map of the 31 December 2020 (Fig. A2), which corresponds to the end of the period that we considered in our study. ~~Even though Weiler et al., (2021) proposed a compensation method for the signals affected by hot pixels, we preferred to discard all the pixels according a~~ Once the hot pixel is discarded, we apply a "sliding

fit" approach (Goldberg et al., 2013; Feofilov and Stubenrauch, 2019) adapted to Aeolus (Feofilov, 2021), which considers the theoretical shape of the Mie backscatter spectrum. In this approach, a predefined spectral shape function is systematically shifted across each row~~map corresponding to the end of Aeolus mission. Once the hot pixel is discarded, its value is replaced by an interpolated value~~ of the Mie channel detector to find the optimal fit that minimizes the difference between the observed and theoretical spectral profiles, thereby simultaneously determining the Mie peak center frequency and reconstructing the complete spectral radiance values.~~two surrounding pixels. By doing so, we avoid potential false trends caused by a decreasing number of "normal" undamaged pixels with time.~~

2~~b~~) Intensities of the particulate backscatter and molecular backscatter in arbitrary unit.

For each profile and each altitude level, we subtracted the ~~average of the~~ Detection Chain Offset (DCO, more details are given in Fig. A1), the solar background, and compensated for the non-uniform intensity distribution on the Mie spectrometer following Donovan et al., (2024b). Future work could include cross-talk correction. ~~stored in the first two and last two pixels.~~ Then, based on the peak position, we selected eight pixels either to its left or right. The signal retrieved in the pixels corresponding to the peak and the two following pixels are summed and correspond to the particulate backscatter, called $I_{part}(z_{L1A})$ here after, z_{L1A} being the altitude of the centre~~center~~ of a layer in a L1A profile. The signals retrieved in the six remaining pixels are summed and correspond to the molecular backscatter, called $I_{mol}(z_{L1A})$. Although the molecular or Rayleigh signal in this approach does not represent the actual molecular backscatter, it is proportional to it, enabling us to use the difference between $I_{part}(z_{L1A})$ and $I_{mol}(z_{L1A})$ to determine the cloud mask.

3~~c~~) Constant vertical and horizontal resolutions.

To detect clouds consistently at all locations and all times, we need the intensities of the molecular and particulate signals at a fixed vertical and a fixed horizontal resolutions. Indeed, variations in the resolutions influence these quantities because a different volume of the atmosphere is probed. Aeolus L1A profiles have a fixed horizontal resolution (3 km) but a variable vertical resolution along the orbit. As the number of layers along the vertical is fixed (24 bins) but the altitudes of the top of the vertical profiles vary between 15 and 25 km, the vertical resolution Δz_{L1A} of Aeolus L1A layers varies along the orbit and ranges between 500 m in the boundary layer and ~~250 m near the surface~~ up to 1~~2~~ km in the free troposphere (Reitebuch et al., 2018). To detect clouds consistently at all locations and all times, we linearly interpolate the molecular and particulate ~~backscattered~~ signals at a fixed vertical resolution of $\Delta z = 480$ m, similar to the one used in CALIPSO-GOCCP (Chepfer et al. 2010), from the sea-level up to 19.2 km of altitude. These new proxies are noted $I_{part\text{-}alt}(z)$ and $I_{mol\text{-}alt}(z)$ and are defined as :

$$I_{part-alt}(z) = I_{part}(z_{L1A}) \frac{480}{\Delta z_{L1A}}$$

(1)

$$I_{mol-alt}(z) = I_{mol}(z_{L1A}) \frac{480}{\Delta z_{L1A}}$$

(2)

where z is the altitude of the centre of a 480 m layer in the new vertical scale. Note that the choice of a 480 m vertical resolution implies possibly losing portions of gradients from the original Aeolus dataset due to altitude mismatches in the original and re-sampled datasets.

where *z* is the altitude of the center of a 480 m layer in the new vertical scale.

4d) Depolarization correction.

ALADIN's emission is circularly polarized but the receiver is only able to measure the co-polarized component of the backscattered light. It misses the cross-polarized component. Backscattering by non-spherical particles modifies the state of polarization of light. Therefore the intensity of the particulate backscatter measured by ALADIN is underestimated within mixed phase clouds and ice clouds that contain non-spherical particles. To compensate for this, we use a monthly climatology of the depolarization ratio (δP) from CALIOP/CALIPSO observations (Feofilov et al., 2022 2024) to correct $I_{part-alt}(z)$ as follows :

$$I_{part-alt-\delta P}(z) = \frac{I_{part-alt}(z)}{(1 - \delta P)},$$

(3)

The output files at this stage are thus orbit files containing profiles of proxies of particulate $I_{part-alt-\delta P}(z)$ and molecular backscatter $I_{mol-alt}(z)$ at a fixed resolution of 3 km along orbit track and resampled at 480 m vertically from the surface up to 19.2 km of altitude.

5) Cloud detection.

For each profile, a layer is declared cloudy when $I_{part-alt-\delta P}(z) - I_{mol-alt}(z)$ exceeds a certain threshold. And aerosol layers are classified as clear sky. More details about the calculations of the threshold are given in appendix A and Fig. A3.

f) Cloud detection.

For each profile, a layer is declared cloudy when $I_{part-alt-\delta P}(z) - I_{mol-alt}(z)$ exceeds a certain threshold. More details about the calculations of the threshold are given in appendix A and Fig. A2.

6e) Fully attenuated bins

Below an opaque cloud, the laser is fully attenuated, making it impossible to retrieve valuable information, neither for the cloud detection, nor for the wind. For each profile containing a cloud, we evaluate $I_{mol-alt}(z)$ at each layer between the surface and 1 km below the lowest cloudy layer. If $I_{mol-alt}(z)$ at each layer is inferior to the noise level, all the layers between the surface and the lowest cloudy layers are flagged as fully attenuated. Otherwise, they are flagged as clear sky. For each orbit the noise level is simply defined as three times the standard deviation of $I_{mol-alt}(z)$ between 60°S and 40°S and between 16 and 18 km of altitude.

For each profile, all the layers located below the lowest cloudy layer with a total backscatter $I_{part-alt-\delta P}(z) + I_{mol-alt}(z) = 0$ are flagged as fully attenuated.

At this stage, the output files are orbit files containing a cloud mask at a 3 km along-track resolution and a 480 m vertical resolution as shown later (Fig. 5b).

At this stage, the output files are orbit files containing a cloud mask at a 3 km along-track resolution and a 480 m vertical resolution. An example is given later in this paper (Fig. 8b)

7g) From cloud mask orbits, we compute daily gridded profiles of cloud fraction over 2° latitude x 2° longitude grid boxes. For each 480 m thick layer, the cloud fraction is the ratio between the number of "cloudy" bins encountered within the grid box for the considered day at this vertical level, and the total number of non-attenuated bins observed within the same grid box at the same vertical level as described in Chepfer et al., (2010).

2.2 Evaluation of Aeolus clouds against a CALIPSO-GOCCP climatology

2.2.1 CALIPSO-GOCCP dataset

To assess the quality of our cloud detection, we compare it to independent cloud observations retrieved from another space lidar. The GCM Oriented CALIPSO Cloud Product from the Cloud-Aerosol Lidar and Infrared Pathfinder Satellite Observation, (CALIPSO-GOCCP, Chepfer et al., 2010) displays cloud profiles at a 333 m horizontal resolution and a 480 m vertical resolution from 2006 to 2023, and thus, overlaps the Aeolus mission during over 4 years between 2018 and 2023. We used CALIPSO-GOCCP version 3.1.4, in which low laser energy shots are discarded. An in-depth comparison between CALIPSO-GOCCP and Aeolus clouds has already been done (Feofilov et al., 2022) but using scattering ratios derived from Aeolus Level 2A calibrated optical properties data (instead of L1A data here) at a coarser resolution of 87 km along orbit track. Even though CALIOP is also a space lidar, differences between CALIOP and ALADIN listed hereafter lead to differences in cloud detection that need to be kept in mind in the comparison:

- CALIOP (Winker et al., 2004) operates at 1064 and 532 nm while ALADIN operates at 355 nm.

- CALIOP points at 3° off-nadir while ALADIN points at 35° off-nadir.

- CALIPSO follows a sun-synchronous orbit, with its ascending (resp. descending) equatorial crossing occurring at 1330 LT (resp. 0130 LT), while Aeolus ascending and descending equatorial crossings respectively occur at 1800 LT and 0600 LT. Therefore, close co-locations between the two instruments are rare, and the diurnal cycle of clouds (Noel et al., 2018; Chepfer et al., 2019), is corrected using the Cloud–Aerosol Transport System (CATS) onboard the International Space Station (McGill et al., 2015) data applied to CALIPSO-GOCCP between 60°S and 60°N as detailed in Feofilov et al., 2022.

- CALIOP is polarization-sensitive, ALADIN is not although we compensate the particulate backscatter by a climatology of the depolarization ratio observed by CALIOP.

- In GOCCP, the bin encompassing the surface can contain information about its cloudiness while it is systematically discarded with Aeolus.

- The horizontal along orbit track resolution is 333 m for CALIPSO-GOCCP and 3 km for Aeolus. For a consistent comparison between the two instruments, we build the CALIPSO-GOCCP-COARSE dataset, whose spatial resolution is set to the same as Aeolus (3 km) prior to the cloud detection.

2.2.2 Comparison of Aeolus and CALIPSO-GOCCP-COARSE cloud climatology
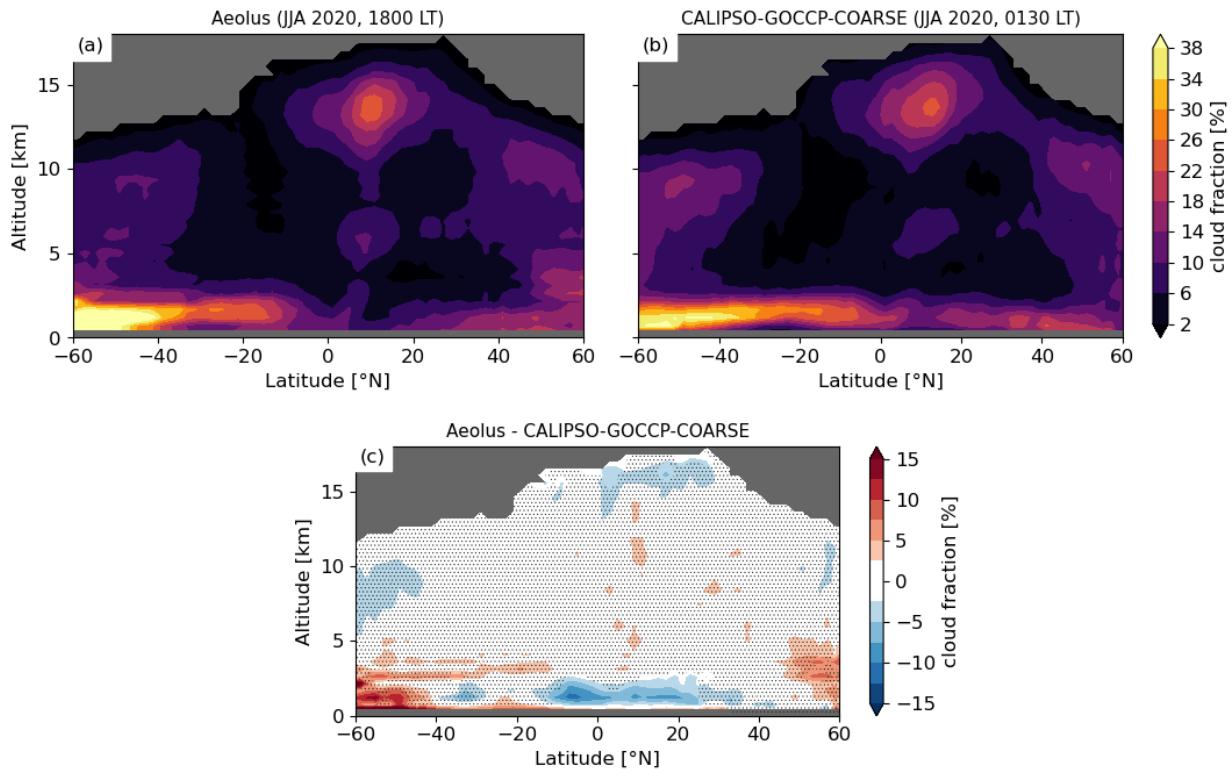
295   **Figure 2: Zonal average cloud fraction profiles for (a) Aeolus at 1800 LT and (b) CALIPSO-GOCCP-COARSE at 0130 LT corrected for the diurnal cycle (c) is the absolute difference of cloud fraction between Aeolus and CALIPSO-GOCCP-COARSE. Non-significant differences (two sided T-test with p-values > 0.05) are dotted. The lowest bin encompasses the surface and is discarded in this study (opaque gray bar). Cloud fractions < 1% are masked in gray.**

We compare the zonal average of cloud fraction profiles retrieved from ALADIN (Fig. 2a) to those retrieved from
300   CALIPSO-GOCCP-COARSE (Fig. 2b) between June and August 2020. Overall, CALIPSO-GOCCP-COARSE and Aeolus show similar cloud patterns. The cloud fractions are in good agreement with R^2=0.84~~0.79~~ and Pearson correlation of 0.92~~0.86~~. In both cases a local maximum of cloud fraction of about 25-30% are found around 10° N within the inter tropical convergence zone (ITCZ), between 12 and 15 km. Minima of cloud fractions with Aeolus and CALIPSO-GOCCP-COARSE appear within the tropical region on each side of the Equator in the middle troposphere, within the descending branch of
305   Hadley circulation. In Fig. 2c, we see that cloud fraction differences remain lower than 2.5% within most of the troposphere and are non-significant almost everywhere (two sided T-test with p-values > 0.05, dotted bins). Below 2 km of altitude and between 10°S-25°N, Aeolus retrieves cloud fraction about 5-10 % smaller (significant) than CALIPSO-GOCCP-COARSE between 30°S and 10°S, the laser of Aeolus being more often fully attenuated in the free troposphere by high clouds. ~~In Fig. 2c, we see cloud fraction differences remain lower than 3 % within most of the troposphere between 60°S and 60°N.~~

310   ~~Between 1 and 2 km of altitude, Aeolus retrieves a zonal mean cloud fraction about 15 % greater than CALIPSO-GOCCP between 30°S and 10°S. These latitudes are dominated by sparse cumulus clouds with horizontal extents smaller than 3 km. In the presence of such small clouds, CALIPSO-GOCCP sees a succession of profiles with sometimes a cloudy layer and sometimes only clear sky layers, while Aeolus only sees a 3 km profile with a cloudy layer. The effect of a coarsened horizontal resolution on cloud detection is more detailed in Chepfer et al., 2013 with cloud fractions 20 to 25 % larger for~~
315   ~~trade wind cumulus when coarsening the resolution (averaging the signal prior to cloud detection) from 330 m to 10 km, which is in the range of what we find in Fig. 2a.~~

320

325

330

335

3 Processing Aeolus winds

The wind profiles from Aeolus Level 2B (L2B) scientific wind product have been continuously validated during the mission with airborne lidars (Lux et al., 2020; Witschas et al., 2020; Witschas et al., 2022), ground based lidars, radars and radiosondes (Ratynski et al., 2023; Iwai et al., 2021; Belova et al., 2021; Baars et al., 2020). So far, Aeolus wind data (L2B) provided to the community are orbit files that contain 2 types of wind profiles (the Mie wind and the Rayleigh wind) estimated from the molecular and particulate backscattered signals respectively. The latest validation campaigns of Aeolus showed that the systematic error (bias) for wind measurements remained within the mission requirements of 0.7 ms^{-1} for both Mie and Rayleigh channels, while the random error was about 3 ms^{-1} for the Mie channel and 5 to 7 ms^{-1} for the Rayleigh channel. This study benefits from the latest reprocessing of L2B Baseline 16.

The Mie and Rayleigh wind profiles have a varying vertical resolution (500 m to 1 km) but also a varying horizontal resolution (ranging from 3 km to 15 km in the Mie channel and fixed at 87 km in the Rayleigh channel). Having a dataset with Aeolus wind profiles resampled at the same fixed resolution as Aeolus cloud profiles is crucial to ease the use of these data for wind cloud interaction studies. In this section we explain how we merge these two wind datasets making use of the cloud mask defined in Sect. 2. In a nutshell, our method consists in re-sampling Rayleigh and Mie winds by interpolating them at the same resolution as the cloud mask (3 km horizontally along orbit track and 480 m vertically), and then selecting the right wind (Rayleigh or Mie) based on the result of the cloud mask (clear or cloudy).

3.1 Re-sampling clear and cloudy sky winds and unifying them on a spatially regular curtain based on our cloud detection

We process the L2B Mie and Rayleigh wind profiles in three successive steps.

1) We first apply the prescribed quality controls for Aeolus L2B winds. We make sure that we only select the valid Mie winds (*validity_flag* = 1, *observation_type* = 1, "cloudy", *hlos_error_estimate* < 5 ms^{-1}) and the valid Rayleigh winds (*validity_flag* = 1, *observation_type* = 0, "clear", *hlos_error_estimate* < 9 ms^{-1}). The *validity_flag* ensures that the wind data have a sufficient quality. The *observation_type* flag filters out Mie wind observations when particulate backscatter is weak (no aerosols nor clouds) and filters out Rayleigh wind observations in the presence of strong particulate backscatter (clouds or aerosols). The *hlos_error_estimate* flag filters out gross outliers (Iwai et al., 2021; Lux et al., 2022).
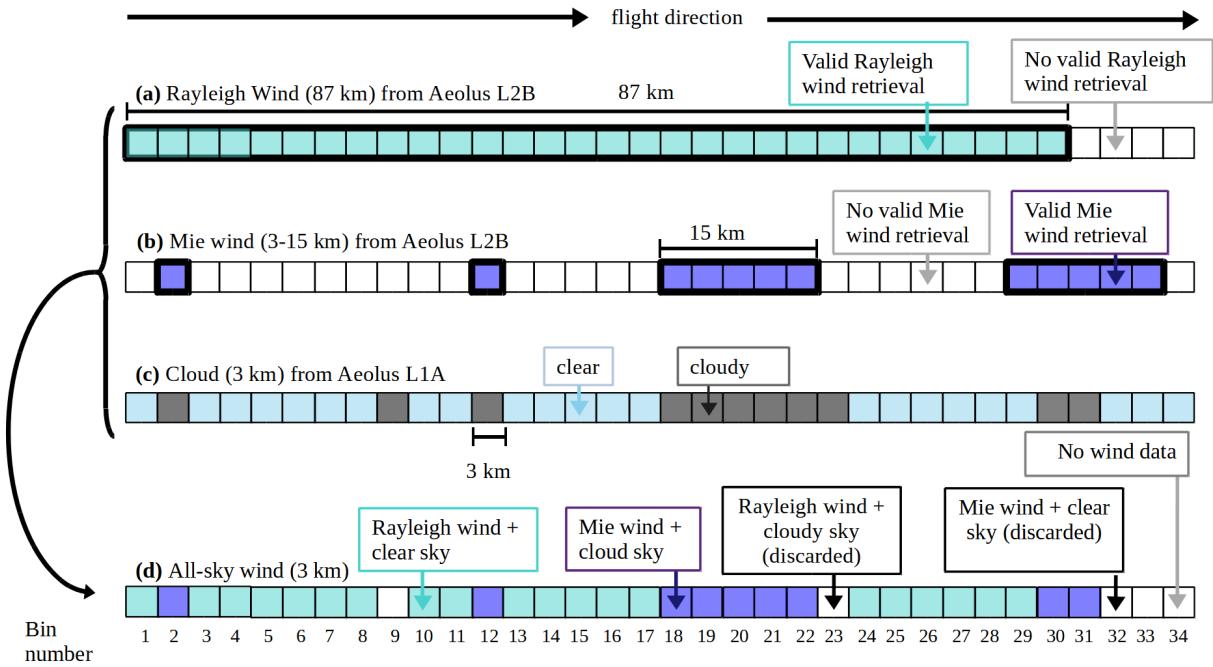
Figure 3: Building the all-sky wind along an orbit segment at one altitude level by selecting the adequate wind from Aeolus L2B based on the cloud detection. Each square represents a bin of 3 km x 480 m. (a) Blue bins contain valid wind from Aeolus L2B Rayleigh channel (87 km 87km resolution along orbit track). (b) Purple bins contain valid wind from Aeolus L2B Mie channel (3 to 15 km resolution along orbit track). (c) Cloud detection made from Aeolus L1A (3 km resolution along orbit track). (d) Aeolus all-sky wind at 3 km along orbit track resolution, built by compositing lines (a) to (c). Blue bins contain a valid clear sky wind, purple bins contain a valid cloudy sky wind and white bins contain no wind data.

2b) We then display each wind at a fixed resolution of 3 km x 480 m. For each 3 km x 480 m bin, we look for the spatially closest L2B Rayleigh wind, evaluated in latitude along the orbit track and in altitude relative to the bin center (Rennie et al., 2020) in wind from the Rayleigh channel in a limit of 87 km, which corresponds to the horizontal resolution of Rayleigh wind observations. We, and we duplicate its value on the 3 km x 480 m orbit file (Fig. 3a) before performing a 2D linear interpolation with a sliding average. The sliding window has the resolution of the original L2B Rayleigh wind observations of Aeolus (87 km horizontally and 500 m to 1 km vertically). Similarly, we look for the spatially closest L2B Mie wind wind from the Mie channel in a limit of 15 km, which corresponds to the maximum horizontal resolution for the Mie wind. We, and we duplicate its value (Fig. 3b) before performing a 2D linear interpolation with a sliding average. The sliding window has the resolution of original L2B Mie wind observations of Aeolus (3 to 15 km horizontally and 500 m to 1 km vertically). We thus obtain at this stage winds from both channels re-sampled at 3 km along track and 480 m vertically. A bin can

contain either a Rayleigh wind (bin 26, Fig. 3a) or a Mie wind (bin 32, Fig. 3b) or both winds (bin 2, Fig. 3a and 3b) or no wind (bin 34, Fig. 3a and 3b). ~~in the fully attenuated bins.~~

3c) Making use of the cloud mask (Fig. 3c), we select for each bin, either a Rayleigh (Fig. 3a) or a Mie (Fig. 3b) wind to build the all-sky wind. Consider bin 2, (Fig. 3) where both Rayleigh and Mie winds coexist. As a cloud was detected (bin 2, Fig. 3c), we select the Mie wind as an element of the all-sky wind (bin 2, Fig. 3d). For bin 29, both Rayleigh and Mie winds also coexist, however, the sky is flagged as clear, ~~no cloud is detected locally~~ so we select the Rayleigh wind as the all-sky wind (bin 29, Fig. 3d). For bin 23 where a cloud is detected, with a Rayleigh wind but no Mie wind, we decide to report "no data" in the all-sky wind dataset instead of a Rayleigh wind (bin 23, Fig. 3d). In a similar way, for bin 32 which shows no Rayleigh wind but a Mie wind in clear sky conditions, we report "no data" instead of a Mie wind (bin 32, Fig. 3d). If a bin is flagged as fully attenuated but a wind was retrieved, it is discarded. By doing so, we ensure that the Rayleigh winds indeed correspond to clear sky situations and the Mie winds to cloudy sky situations, consistently with our cloud mask. ~~From now on, we will simply call these winds "clear sky wind" and "cloudy sky wind", the all-sky wind being thus a merging of both of them.~~

The following statistics illustrate how often Rayleigh winds are substituted by colocated Mie winds when clouds are detected, and the differences between the two winds. During the period extending from June to August 2020, 83% of the 3 km x 480 m bins flagged as cloudy with our cloud detection contained both a Rayleigh and a Mie wind, while 10% of bins flagged as cloudy contained only a Mie wind and 7% only a Rayleigh wind (on the edge of clouds or at cloud tops). On the other hand, 92% of bins flagged as clear contained only a Rayleigh wind, 7% contained both a Mie and a Rayleigh wind and 1% contained a Mie wind only. For cloudy bins where both Mie winds and Rayleigh winds coexist, the average difference between Mie and Rayleigh wind is -0.20 ms^{-1} from June to August 2020 (Fig. B2). This small systematic difference is reassuring as the winds are perfectly co-located in the cloud, however, the standard deviation of the differences is quite large at 5.38 ms^{-1}. This is essentially a consequence of the random error on wind observations (approximately 5 ms^{-1} for the Rayleigh winds and 3 ms^{-1} for the Mie winds) and the (at least) 5 times finer native horizontal resolution of the Mie winds compared to the Rayleigh winds. The substitution of Rayleigh winds by Mie winds in cloudy sky will therefore improve the study of wind-cloud interactions.

As this study is limited to the range 60°S – 60°N and as the laser pointing direction of Aeolus within this latitude range is quasi-eastward during ascending orbit and quasi-westward during descending orbit, (Fig. 1, Krisch et al., 2022), the HLOS wind observed by Aeolus, that is often noted v_{HLOS} in the literature, is simply noted "u" all along the paper for simplicity. We adopt the convention that u is negative (positive) when the wind is westward (eastward). We use u_{cloud} (u_{clear}) to denote Mie

(Rayleigh) winds filtered by the cloud (clear sky) mask while u_{allsky} is the merging of both u_{cloud} and u_{clear}. At this stage, the output files are individual orbit files with a cloud mask and Aeolus cloudy, clear and all-sky winds at 3 km along-track resolution and 480 m vertical resolution.

d) Under a cloudy layer, the Rayleigh signal is so weak that the clear sky wind retrieval can not be trusted. For each profile, we therefore discard all clear sky winds located at altitudes below a cloudy layer.

At this stage, the output files are individual orbit files with a cloud mask and Aeolus cloudy, clear and all-sky winds at 3 km along-track resolution and 480 m vertical resolution.

3.2 About the sub-grid variability of wind at 3 km

At a given altitude, each 87 km ~~the re-sampling procedure (Sect. 3.1) duplicates 30 times each~~ clear sky wind is horizontally resampled at ~~observation at 87 km on a~~ 3 km ~~grid~~ (Fig. 3a, 3d). If clear sky winds were homogeneous over 87 km, this operation would lead to accurate winds~~results~~ at a resolution of 3 km, but it is a source of inaccuracies when the sub-grid variability (below 87 km) of clear-sky winds is large. To quantify this error, we use two independent datasets, from an aircraft and from a high resolution model.

First, we use profiles of wind acquired using an airborne 2µm Doppler Wind Lidar (DWL) operated by the German Aerospace Center (DLR) onboard a Falcon aircraft during the AVATAR-T validation campaign of Aeolus. This Lidar has a spatial resolution of 200 m horizontally and 100 meters vertically, extending between the surface and the aircraft which usually flies at about 10 km to 11 km of altitude. To retrieve the horizontal wind, an azimuth scan is applied and takes about 42 s, leading to a horizontal resolution of about 8 km (Witschas et al., 2017, 2022). The systematic error of horizontal wind measurements is estimated to be 0.1 ms^{-1} and the random error about 1 ms^{-1}. A total of 8250 km was scanned by the aircraft near Cape Verde during the 5 flights we selected. A first selection is made to discard bins with an uncalibrated backscatter superior to 500 (that we estimated a good threshold to discriminate clear and cloudy sky). We first project the wind as if it was observed by Aeolus during its descending orbit and we average the wind vertically to a resolution similar to that of the Aeolus dataset, 480 m~~Aeolus of 500 m (5 consecutive bins vertically in a single profile). We then extract from the curtain segments of 500 m vertically x 88 km horizontally (11 consecutive profiles), the closest from Aeolus clear sky observations. A total of 94 independent segments were sampled with 11 consecutive bins with valid wind measurements in clear sky conditions. For each segment, we calculate the standard deviation of the wind within the segment. A standard deviation equals to zero means that there is no horizontal "sub-grid" variability of the wind, and thus, the coarse resolution of Aeolus does not miss any sub-grid atmospheric circulation. The higher the standard deviation, the more sub-grid circulations are missed by Aeolus, making the re-sampling of the winds from 87 to 3 km questionable. We observed that in 97 % of the clear sky segments, the standard deviation of the wind within the segment is lower than 2 ms^{-1} and in 83 % of the segments, it is lower than 1 ms^{-1} (Fig. 4). This stresses out that when re-sampling the clear sky wind from 87 to 3 km, a sub-grid variability of about 1 ms^{-1} is lost within the clear sky segment.~~

We then extract 11 adjacent 8 km x 480 m airborne DWL wind values within a curtain segment of 87 km horizontally x 480 m vertically to replicate Aeolus clear sky observations. ~~We then extract from the curtain segments of 500 m vertically x 88 km horizontally (11 consecutive profiles), the closest from Aeolus clear sky observations.~~ A total of 94 independent segments were sampled with valid wind measurements in clear sky conditions. We calculate the standard deviation of the wind within each segment. A standard deviation equals to zero means that there is no horizontal "sub-grid" variability of the wind, and thus, the coarse resolution of Aeolus does not miss any sub-grid atmospheric circulation. The higher the standard

deviation, the more sub-grid circulations are missed by Aeolus, making the re-sampling of the winds from 87 to 3 km questionable. We observed that in 97 % of the clear sky segments, the standard deviation of the wind within the segment is lower than 2 ms^{-1} and in 80~~83~~ % of the segments, it is lower than 1 ms^{-1} (Fig. 4). This stresses out that when re-sampling the clear sky wind from 87 to 3 km, a sub-grid variability of about 1 ms^{-1} is lost within the clear sky segment. Note that AVATAR-T wind observations are geographically limited around Cape Verde, but the wind encountered in this region are representative of a tropical marine trade winds regime (77 % of the Tropics, 40 % of the global surface) throughout most of the year (Bernardino et al., 2018).

To get even closer to the actual re-sampling resolution, we used a WRF simulation (more details about this simulation can be found in Ban et al., 2021) over Europe with a horizontal resolution of 3 km in clear sky. The domain is about 1200 km by 1500 km wide and tilted westward by about 8 degrees. This configuration means that the "latitude" axis of the domain is aligned with typical ascending orbit tracks of Aeolus. This allows us to repeat the procedure described above for the 2µm DWL with the WRF simulation. A total of 375 independent segments of 87 km horizontally x 480 m vertically were sampled with clear sky only. We limited the domain vertically to 10 km to stay consistent with the airborne observations. The sub-grid variability of the horizontal wind is found to be similar to that observed by the DWL with 90~~95~~ % of the segments having a sub-grid variability of less than 2 ms^{-1} and 75~~86~~ % of the segments less than 1 ms^{-1}. When extending the analysis of the WRF simulation up to 19 km (similar to the maximum altitude reached by Aeolus in our dataset, Fig. B3), the variability of the horizontal wind is even less, with 99 % of the segments having a sub-grid variability inferior to 2 ms^{-1} and 93~~90~~ % of the segments less than 1 ms^{-1}. The alpine region sets a high bound for horizontal wind variability as it is influenced by a large amount of gravity waves which induce perturbations of the horizontal wind of 1-2 ms^{-1} on scales of 20-60 km (Hierro et al., 2018). With WRF the conclusions are the same that with the airborne DWL (which is noisy but coarser). Overall, a natural sub-grid variability of about 1 ms^{-1} is missed by the coarse resolution of Aeolus, making atmospheric circulations of horizontal scale smaller than 87 km and with winds less than 1 ms^{-1} in clear sky segments non observable. However, it is possible to study circulations at a 3-15 km horizontal scale in cloudy conditions and to compare them to the spatially closest clear sky observations, provided that we increase the uncertainty measurement in clear sky conditions by 1 ms^{-1} to take account of the non-observed sub-grid variability. Section 4.3 is dedicated to such comparisons at cloud scale.

520

525

530

Figure 4: Standard deviation of the wind speed within a segment of 87 km as observed by the airborne DWL with a horizontal resolution of 8 km and from a WRF model scene with a horizontal resolution of 3 km. DWL and WRF wind profiles are averaged vertically to a resolution of 480 m, similar to our Aeolus dataset. All altitudes between the surface and 10 km are included.

535

540

545

550

3.3 Case study of the tropical cyclone Paulette observed with Aeolus

Figure 5 illustrates how Aeolus resampled cloud mask and winds allow us to observe from space different features ranging from cyclones to cumulus clouds. For a general audience, the most famous phenomenon associating clouds and winds is certainly the cyclone. This mesoscale system that develops over warm oceans combines both an opaque cloud cover that can be observed from space (Fig. 5a) and very fast winds around its center. During its lifetime, Aeolus observed multiple cyclones, sometimes crossing them near their centre (Marinescu et al., 2022). Figure 5a shows an example of intersection between Aeolus and the tropical cyclone Paulette over the Atlantic Ocean during the hurricane season cyclic season, on 12 September 2020. The wind and cloud curtains are displayed between 20°N and 40°N. Note that Aeolus covers this distance in about 4 minutes, so the curtains represent a snapshot of the scene. The cyclone is identified by the continuous high cloud cover between 20°N and 32°N at about 12 km of altitude (Fig. 5b). The laser typically only penetrates 1 to 2 km below the uppermost cloudy layer of the cyclone allowing us to observe the cloudy sky winds at the top of the cyclone, near the outflow level (Fig. 5c). About 2 km below the uppermost cloudy layer, the attenuation of the laser (Fig. 5b) prevents us from retrieving information about the wind below. However, Aeolus observes the clear sky winds surrounding the cyclone, typically from the surface to 18 km of altitude. The cross section of the clear sky winds (Fig. 5d, but also visible Fig. 5e) reveals the wind shear found where counter-clockwise winds around the cyclone base meet the clockwise winds at the top of the cyclone. This happens at about 8 km of altitude at 25°N and 35°N. The further we look from the cyclone, the higher in altitude the reversal of the wind occurs. Note that in the paper, we use the convention that eastward winds are positive and westward winds are negative. More details are given Fig. B1.

The case study visually illustrates how noisy the wind measurements are, especially in clear sky (random error of about 5 ms^{-1}) and to a fewer extent in cloudy sky (random error of 3 ms^{-1}). One should remember that after the high resolution resampling of the winds, a temporal or spatial averaging is necessary to reduce the random error of Aeolus wind measurements.

This particular case study is also interesting as it encounters a diversity of clouds. We observe shallow cumulus clouds (Fig. 5b) between 20°N and 23°N, with their tops below 3 km and sometimes only occupying a single profile and surrounded by clear sky profiles. This stresses out the importance of performing cloud detection at full horizontal resolution of 3 km. We also observe cirrus clouds, northward of the cyclone, extending from 33°N to 34°N and between 12 and 15 km of altitude. Along half of its length, this cirrus does not fully attenuate the laser as some clear sky layers can be retrieved below its base.
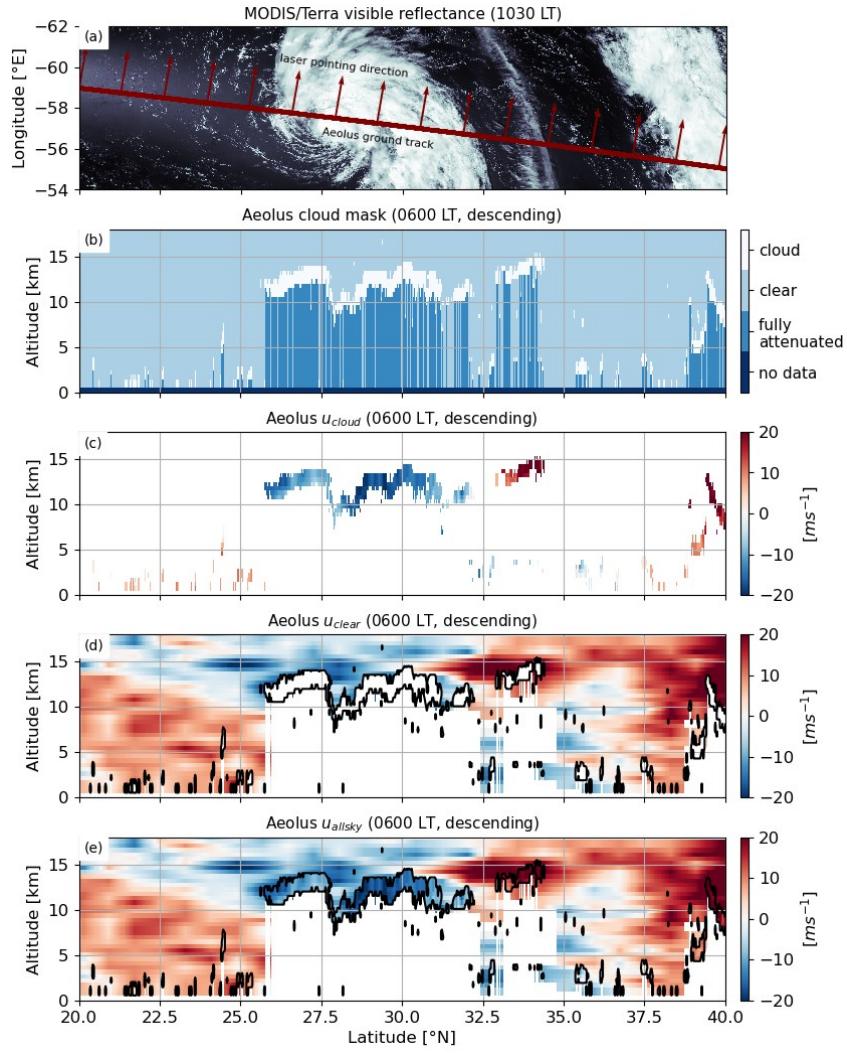
Figure 5: (a) Descending orbit segment crossing the tropical cyclone Paulette over the Atlantic ocean (2020-09-12T09–2020-09-12T11) plotted in red over a MODIS/Terra reflectance image. The red arrows represent the laser pointing direction. **(b)** Aeolus cloud mask. Aeolus wind **(c)** in cloudy sky **(d)** in clear sky and **(e)** in all-sky. Aeolus winds are negative when blowing westward and positive when blowing eastward. In (b), (c), (d) and (e), the resolution of the re-sampled data is 3 km horizontally and 480 m vertically.

4 Results at different scales

In this section, we illustrate analyses with our observations through three examples at different spatial scales: large, regional and cloud scale inferior to 100 km.

4.1 Global-scale circulations observed with Aeolus
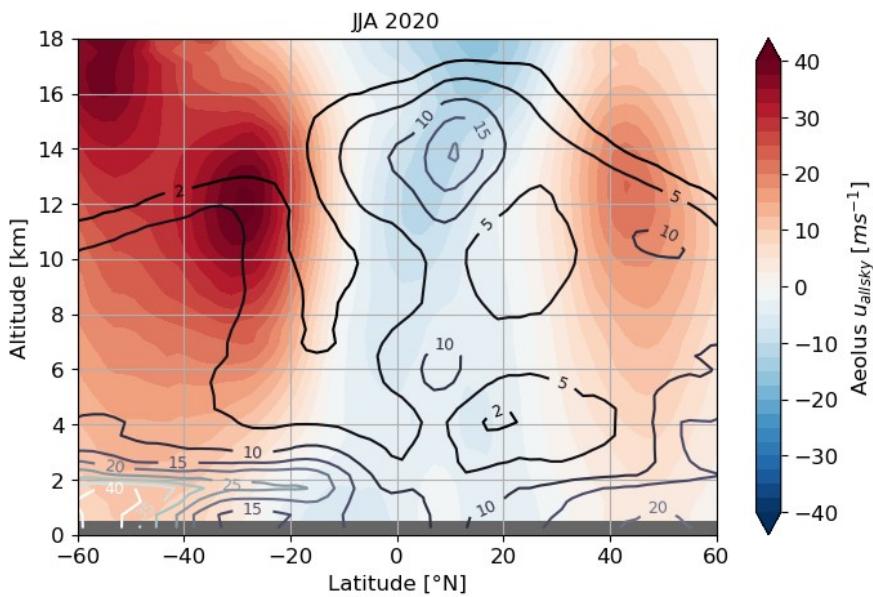
Figure 6: (a) Zonal average of all-sky wind speed profiles from June to August 2020. Contours represent the zonal average cloud fraction. ~~Contours represent the fraction of re-sampled winds retrieved in cloudy sky to the total number of re-sampled winds (clear + cloudy sky winds). Latitudes higher than 60° are shaded as the laser is not pointing in a zonal direction (Fig. 1).~~

Aeolus observes the main features of the general circulation, like for example the trade winds below 2 km of altitude

 between 20°S and the equator and from 10°N to 20°N (Fig. 6) and the subtropical jet streams at 30°S and 40°N with their cores located at 12 km of altitude. As this zonal average of wind profiles is calculated from June to August 2020, the polar stratospheric jet is visible around 55°S and 17 km of altitude. Moreover, the speed of the subtropical jet stream in the southern hemisphere is larger than 35 ms^{-1} due to a large meridional temperature gradient in the winter hemisphere through thermal wind balance, while the northern hemisphere subtropical jet stream only reaches 25 ms^{-1}.
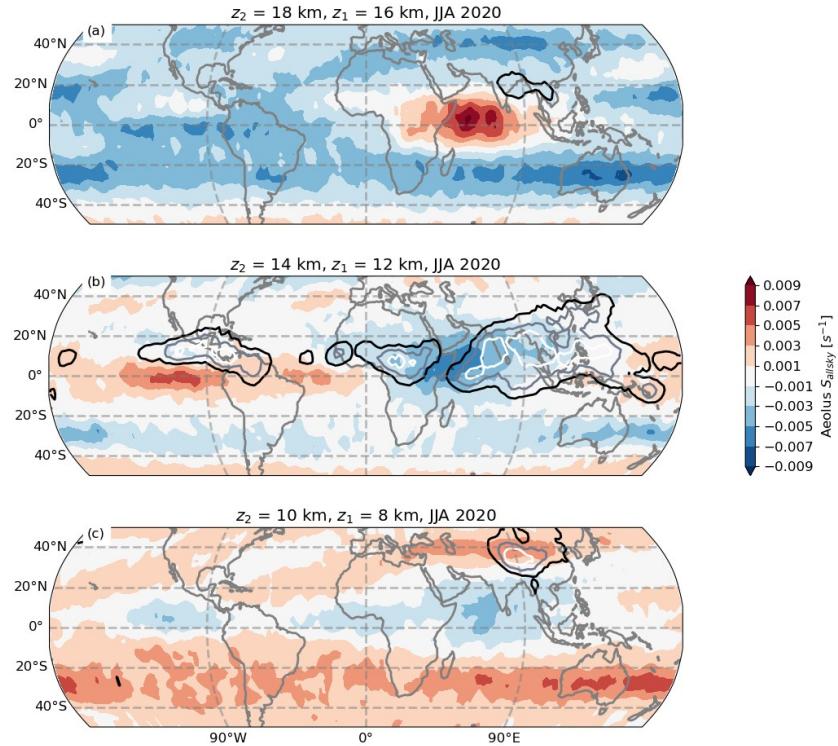
Figure 7: Map of the median wind shear S$_{allsky}$ calculated a) between 8 km and 10 km, b) between 12 and 14 km and c) between 16 and 18 km. Maps are 2° x 2°, from June to August 2020. Contours represent cloud covers of 5, 10, 15 and 20% for each altitude range.

Figure 7 shows maps of the median wind shear S$_{allsky}$ computed between two layers separated by 2 km of altitude (larger than the native resolution of Aeolus) following Eq. 4:

$$S_{allsky} = \frac{u_{allsky}\left(z_2\right) - u_{allsky}\left(z_1\right)}{\left(z_2 - z_1\right)} \tag{4}$$

Figure 7a focuses on the wind shear between 16 and 18 km of altitude, which corresponds to the tropical tropopause. S$_{allsky}$ mostly takes negative values within the tropics between -3×10^{-3} s^{-1} and -9×10^{-3} s^{-1} as the Quasi Biennial Oscillation is in a negative phase (fast westward winds in the stratosphere around z$_2$), but S$_{allsky}$ is positive and up to 1×10^{-2} s^{-1} over the Indian Ocean as the Tropical Easterly Jet (TEJ, Koteswaram, 1958) blows westward up to 40 ms^{-1} at 16 km of altitude during the South-Asian Summer Monsoon (SASM). This region is also subject to deep convection, particularly over the Bay of Bengal (Zuidema, 2003 ; Hemanth Kumar et al., 2015), which then leads to cirrus clouds (Ali et al., 2022) distributed in the upper

half of the troposphere, up to 16 km of altitude. Figure 7a shows that indeed, a cloud cover of 5% is observed between 16 and 18 km of altitude, which corresponds to the highest clouds observed in this region (Ali et al., 2022).

Between 12 and 14 km of altitude (Fig. 7b), the Northern hemisphere exhibits weak wind shear values between -3×10^{-3} and
670 3×10^{-3} s^{-1} except above the Indian Ocean where it reaches -8×10^{-3} s^{-1} just under the core of the TEJ. This maximum of negative wind shear is located between central Africa and continental India, that both show a weaker negative wind shear, as these two regions prone to vigorous deep convection (up to 25% of cloud cover between 12 and 14 km) most likely experience a strong vertical mixing. At this altitude, another maximum of cloud cover is observed above central America, which also peaks at 20 % and results from continental deep convection.

675 In the southern hemisphere, a band of maximum negative wind shear of -3×10^{-3} s^{-1} to -9×10^{-3} s^{-1} is observed along the 30°S parallel. This maximum of negative wind shear is located just above the Sub-Tropical Jet (STJ) whose core's altitude is 12 km (z_1) and reaches up to 40 ms^{-1} while the wind at 14 km does not exceed 30 ms^{-1}.

Between 8 and 10 km (Fig. 7c), the wind shear along the 30°S parallel is positive and reaches 5×10^{-3} s^{-1} as the core of the STJ is located just above. The strong wind shears induced by the STJ are not observed in the northern hemisphere as the
680 meridional temperature gradients (which drive jet streams) are weaker than in the southern hemisphere from June to August. We observe nevertheless wind shears faster than 5×10^{-3} s^{-1} over continents in the northern hemisphere, extending from Turkey to coastal China.

This difference between the two hemispheres is also visible on the map of wind shear through the troposphere (Fig. 7),
685 where S_{tropo} is defined as :

$$-S_{tropo} = \frac{u_{allsky}(z_2 = 10\,km) - u_{allsky}(z_1 = 2\,km)}{(z_2 - z_1)}; \tag{3}$$

The wind shear is here computed between 10 km (within the troposphere between 60°N and 60°S) and 2 km (the typical border between the boundary layer and the free atmosphere), but a similar study can be performed with another choice of altitudes. The wind shear ranges between 1×10^{-3} and 3×10^{-3} s^{-1} in the northern hemisphere while it largely exceeds 3×10^{-3} s^{-1}
690 in the southern hemisphere. During boreal summer, the Indian Ocean exhibits eastward surface winds typical of the monsoon circulation and a Tropical Easterly Jet with a core at 16 km of altitude. This results in the strongest negative wind shear, with values below -3×10^{-3} s^{-1} (wind profile is sheared westward as we go up in altitude). This region is also subject to deep convection (Hemanth Kumar et al., 2015) during this period as well as an important cirrus cloud fraction (Ali et al., 2022). As a result, this is also over the Indian Ocean that Aeolus retrieves the largest proportion of winds in cloudy sky at 10 km of
695 altitude, up to 25 %. Everywhere else in the tropics, between 2 % and 10 % of the winds at 10 km of altitude are retrieved in

cloudy sky, the remaining are retrieved in clear sky. Note also that low fractions of cloudy sky winds (vs all sky winds) correspond in the Northern Atlantic and Pacific Oceans, to regions of strong positive shears (wind profile is tilted eastward as we go up in altitude), up to $3 \times 10^{-3} s^{-1}$ that are typical of a strongly stratified free troposphere.

700

Figure 7: *Map of the wind shear S_{allsky} calculated between z_1=2 km and z_2=10 km at 2° x 2° from June to August 2020. Contours represent the fraction of re-sampled winds retrieved in cloudy sky at 10 km of altitude to the total number of re-sampled winds (clear + cloudy sky winds) retrieved at 10 km of altitude. Latitudes higher than 60° are shaded as the laser is not pointing in a zonal direction (Fig. 1). Schematic on the right illustrates the link between the colorbar used on the wind*
705 *shear map on the left and the typical wind profile associated.*

710

715

720

4.2 Seasonal changes of clouds and winds over the Indian Ocean

During the months of June-August, we observe a maximum of high cloud fraction over the Indian Ocean (Fig. 8e), as well as thea Tropical Easterly Jet (TEJ) that extends from the Tibetan plateau to the Western coast of Africa (Fig. 8f). The core of the TEJ, is located at about 16 km of altitude, . It is visible on the map (maps Fig. 8c) with westward winds exceeding 30 ms^{-1} over the Arabian Sea from June to August 2020 (consistent with Liu et al., 2024). We focused on a small domain located over the Indian Ocean on the Western coast of India and under the influence of the TEJ during summer (black rectangle, Fig. 8a). The domain extent of 20° of longitude ensures that Aeolus crosses it at least twice a day, once ascending and once descending. On the time series of wind profiles (Fig. 8f), the apparition of a westward (negative) winds appear wind speed appears in late May and reachreaches values of above 30 ms^{-1} within a few days only. The jet persistssubsists until the last week of October before decaying rapidly, giving way to eastward winds (positive values) again. It is worth noting that during the same period of the TEJ, Aeolus captures persisting eastward (positive) winds below 2 to 5 km of altitude associated to the monsoon circulation. Figure 8e displays the daily average profiles of the cloud fraction observed by Aeolus over the same domain. The low cloud fraction is persistent during the entire year and above 30 % during early winter over the cold Arabian sea and during late September. We also notice two minima of low cloud fraction which correspond to the reversal of boundary layer winds, in April from westward to eastward dominant winds, and in October from eastward back to westward dominant winds (more visible in Fig. B4). Note that during the weeks preceding and following the reversal of the boundary layer winds in April, low clouds are confined between the surface and 1 km of altitude, while during periods of continuous westward winds (January to March 2020), low clouds typically extend up to 3 km. Part of this seasonal cycle of cloud top height is explained by a cooler Sea Surface Temperature (SST) from January to February, favorable for higher cloud tops (Höjgård-Olsen et al., 2022), and a warmer SST afterwards. Moreover, during the reversal of the winds, the evaporation flux at the surface the Indian Ocean is reduced, resulting in a shallower and dryer boundary layer, less favorable for the formation of low clouds (Mieslinger et al., 2019, Nuijens and Stevens, 2012). We also observe mid-level and high clouds above 5 km and up to 16 km, preferentially occurring between June and October, i.e. when the TEJ is the most active. As this period also corresponds to the South-Asian Summer Monsoon (SASM), the presence of high convective clouds is not surprising. The concurrence of a strong TEJ and monsoon clouds and rainfall was already mentioned by e.g. Koteswaram, 1958. However, deep convective cloud cover accounts for only 9% of the area of the Indian Ocean in July (Massie et al. 2002), and they are mainly located over the Bay of Bengal (Zuidema, 2003), thus the high cloud fraction seen in Fig. 8e between June and October must be essentially made of cirrus, as 90% of them are located outside of regions of deep convection (Massie et al. 2002). The large increase of the cirrus cloud fraction during the period where the TEJ is the most vigorous is thus thought to be favored by horizontal transport of moist air originating from convective late April and late October. The most striking feature is the presence of high clouds above 5 km and up to 16 km, preferentially occurring

between June and October, i.e. when the TEJ is the most active. These high clouds are associated to deep convection and to a
large increase of cirrus cloud fraction, that is favoured by horizontal transport of moist air originating from convective
towers over long distances (Das et al. 2011). However, below and above the core of the TEJ, we observe wind shears larger
than 10^{-2} s^{-1}, which were found to alter cirrus clouds structure and reduce their lifetime (Jensen et al., 2025). Note that the
time of ascending orbits of Aeolus (1800 LT) corresponds to a maximum of deep convection over the Bay of Bengal
(Zuidema, 2003), while descending orbits (0600 LT) occur before the dissipation of cirrus clouds (Ali et al., 2022). Aeolus
observations can thus be of a great help to better understand these interactions between horizontal winds and cirrus clouds
formation.
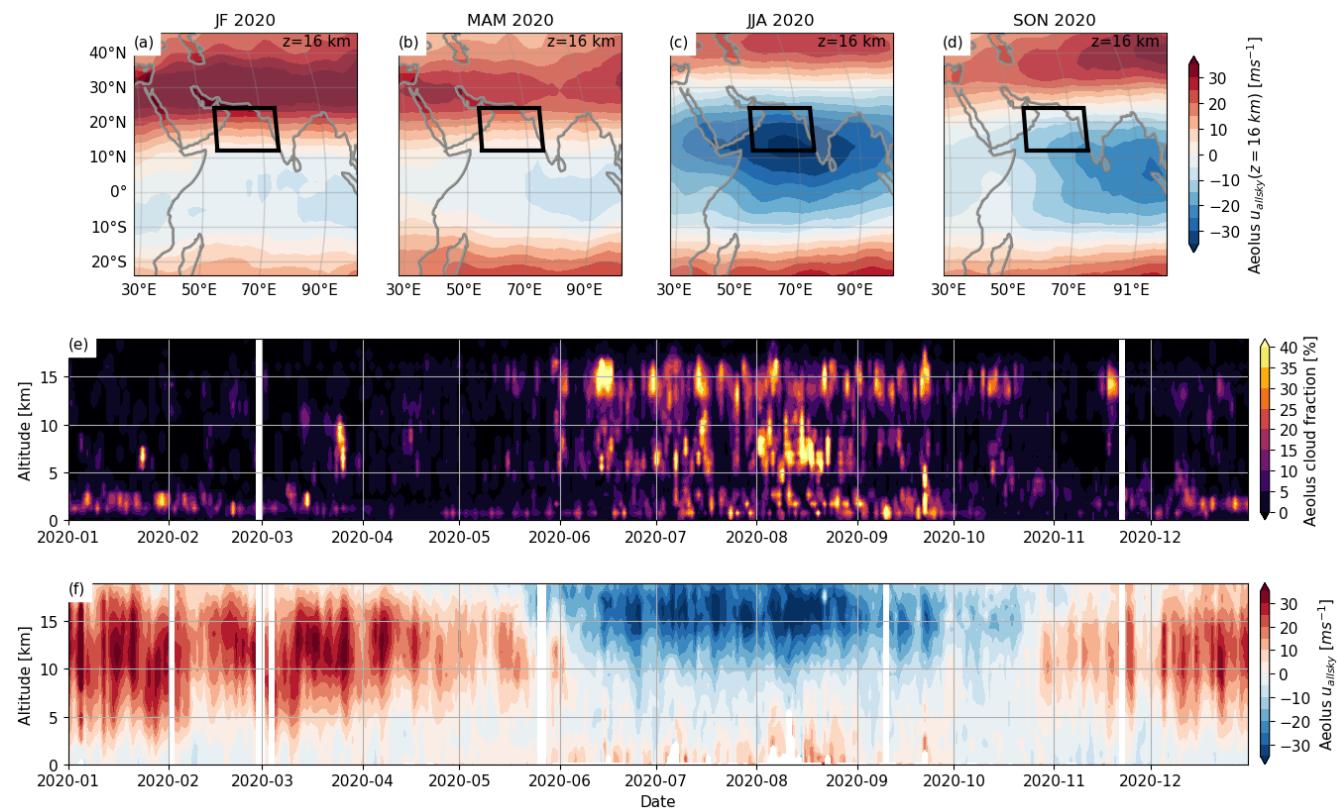
Figure 8: (a) map of the averaged all-sky wind speed $u_{allsky}(z=16$ km) during the months of January and February 2020; (b, c and d) are the same for respectively March-May, June-August and September-November 2020. The rectangle (12°N-24°N, 55°E-75°E) represents a domain selected as it is under the influence of the Tropical Easterly Jet during summer. Time series at a daily resolution of (e) the average profiles of cloud fraction within the domain and (f) the average profiles of all-sky wind speed within the domain.

4.3 Cloud scale circulations inferior to 100 km

When convection is triggered, the horizontal wind from the sub cloud layer is transported vertically within the cloudy layer, leading to different horizontal wind speeds within the cloudy layer and the surrounding environment at a given vertical level. This phenomenon referred as "Convective Momentum Transport" has been studied using Large Eddy Simulations (LES, Siebesma et al., 2003), and more recently using airborne measurements (Koning et al., 2022). In this subsection we investigate the ability of Aeolus to significantly retrieve different wind speeds within a cloud and in the clear sky surrounding the cloud.

4.3.1 Is it possible to capture the differences between wind speeds within clouds and their surrounding clear sky at the resolution of Aeolus?

To test the feasibility of significantly observing different wind speeds within clouds and their surroundings with Aeolus, we use DWL data measured with a Falcon flight during the AVATAR-T campaign. Figure 9 displays an example of cumulus clouds forming near Cape Verde and overflown by the DLR Falcon. We first project the zonal and meridional components of the wind as if Aeolus was observing the scene during its descending orbit. This results in profiles of $u_{DWL, allsky}$ at 100 m vertical resolution and 8 km horizontal resolution (Fig. 9a). We then coarsen the uncalibrated backscatter at the native horizontal and vertical resolutions of Aeolus before interpolating the signal at 3 km horizontal x 480 m vertical resolution, to create a cloud mask (Fig. 9b), consistent with our dataset. In the same way, we coarsen the profiles of $u_{DWL, allsky}$ at the native resolution of Aeolus, before interpolation on the 3km x 480 m grid. We further average the $u_{DWL, allsky}$ profiles encompassing the centre of the cloud between 1280 and 1320 km along flight (Fig. 9c, red curve). Similarly, we average the clear sky wind profiles on the left edge of the cloud, between 1210 and 1275 km along flight, to simulate a portion of clear sky wind observed by Aeolus (Fig. 9c, black curve). ~~We then further averaged the two $u_{DWL, allsky}$ profiles encompassing the edge of the cloud between 1284 and 1300 km along flight and performed a sliding average vertically of 500 m, to replicate the original vertical and horizontal resolutions of Aeolus winds. We averaged the clear sky wind profiles on the left edge of the cloud, between 1210 and 1280 km along flight, to simulate as well as possible a clear sky wind profile viewed from Aeolus. We performed a sliding average vertically of 500 m.~~

We see that between the surface and the Cloud Base Height (CBH) of 960 m, the values of u_{DWL_allsky} are quite similar for a measurement performed just below the cloud base, or in the clear sky surrounding the cloud. In contrast, above 960 m, the clear sky wind is tilted westward and reaches -5 ms⁻¹ at 1.6 km of altitude (corresponding to the Cloud Top Height - CTH), while within the cloudy layer, as air masses from the surface are carried upward within the cloud, the wind only reaches -3 ms⁻¹ at the CTH. At this altitude, the difference between the clear sky wind and cloudy sky winds is the largest and reaches 2 ms⁻¹. Note that Koning et al., (2022) observed horizontal wind differences of up to 5 ms⁻¹ around convective updrafts using airborne wind observations. Between the CBH and the CTH, the wind shear within the cloud is about -5×10⁻⁴ s⁻¹. The wind

shear is larger (in absolute value) in the clear sky surrounding the cloud at the same altitude and is approximately equal to -3.7×10^{-3} s^{-1}. Above the cloud top, cloudy and clear sky wind profiles join again at 2.1 km of altitude. Between the cloud top and 2.1 km, as the wind just above the cloud top experiences drag from the cloud top, the wind shear is negative and maximum in absolute value just above the cloud top, reaching -4.6×10^{-3} s^{-1}, while the wind profile is not sheared in the clear sky surrounding above the CTH.

The case study presented in Figure 9 shows that when averaging the airborne DWL wind data to the coarser horizontal and vertical resolutions of Aeolus, it remains possible to capture significantly different wind speeds within clouds and within their surroundings in shallow convection. This finding encourages us to observe the impact of convective motions on the horizontal wind speed with the Aeolus dataset. However, because of Aeolus wind observations having a larger random error than the airborne DWL wind observations, an averaging of multiple Aeolus wind profiles is necessary to observe significant wind speed differences between the cloud and its surrounding clear sky. ~~The case study presented in Figure 9 shows that even at the coarse vertical and horizontal resolutions of Aeolus, it is possible to capture significantly different wind speeds within clouds and within their surroundings in shallow convection. This finding encourages us to search for evidences of convective momentum transport in our Aeolus dataset.~~
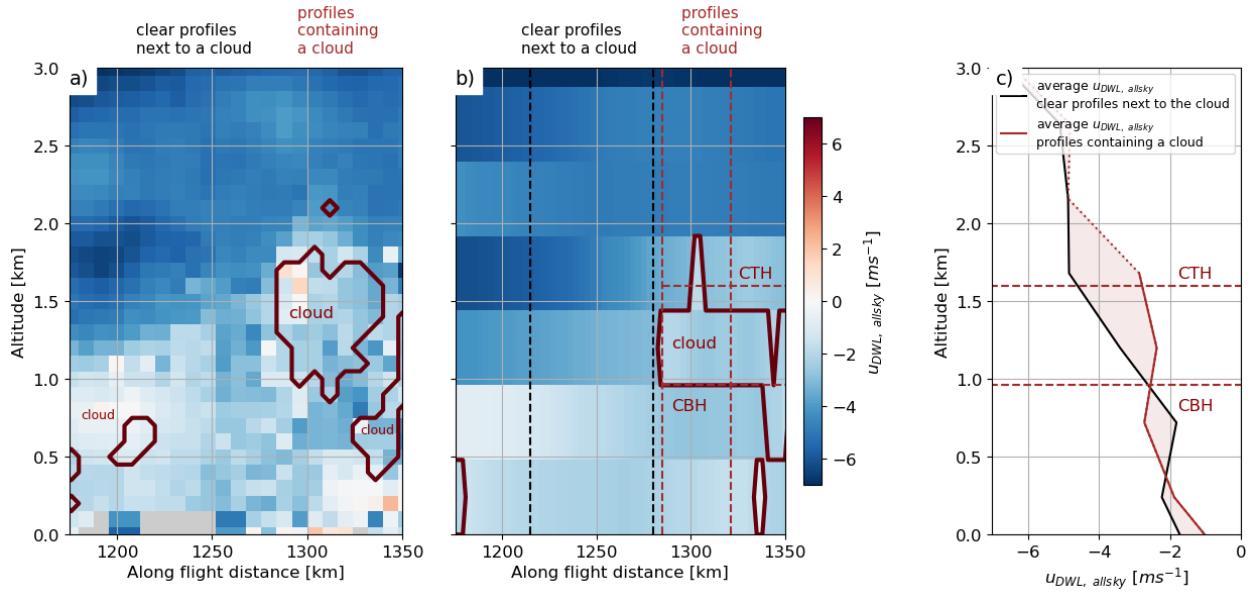
Figure 9: (a) Curtain of $u_{DWL, allsky}$ acquired by the airborne DWL and projected along the laser pointing direction of Aeolus during the AVATAR-T campaign. (b) is the same $u_{DWL, allsky}$ wind curtain coarsened at the resolution of our Aeolus dataset (3 km along flight direction, 480 m vertically). The cloud mask is also coarsened and clouds are represented with solid red contours. Vertical red dashed lines represent the horizontal extent of the profiles encompassing a cloud while vertical black dashed lines represent the horizontal extent of clear sky profiles next to the clouds. Horizontal red dashed lines mark the average Cloud Base Height (CBH) and Cloud Top Height (CTH) for the profiles encompassing a cloud. (c) Profiles of $u_{DWL, allsky}$ encompassing the cloud (red curve) and in the clear sky surrounding the cloud (black curve).

4.3.2 Differences between wind speed within clouds and their surrounding clear sky with Aeolus

We split the study within regions (Fig. 10a) exhibiting different types of clouds and different large-scale circulations and we focus on the entire year 2020. ~~In order to study wind speed differences of only a few ms^{-1}, it is necessary to reduce the random error and therefore average a large number of wind profiles. We chose to split the study within regions exhibiting different types of clouds and different large-scale circulations.~~ The first region is dominated by Stratocumulus decks sometimes transitioning to Cumulus clouds (TrSc). They are prevalent in the eastern subtropical oceans (Wood, 2012) and are capped by a strong inversion, usually created by the large scale subsidence associated with the descending branch of the Hadley-Walker circulation. The inversion is characterised by a sharp transition in most meteorological variables (Wang et al., 2008; Hourdin et al., 2019). The second region is dominated by Cumulus clouds (Cu) (McCoy et al., 2017 ; Qu et al., 2015). Cumulus clouds are usually found in the western subtropical oceans and are associated with a deeper boundary layer compared to the Stratocumulus region (Scott et al., 2010). These two regions are found above oceans and usually under the subtropical jet streams. The Indian Ocean is the third region, thermodynamically more unstable and prone to deep convection, it is also crossed by the Tropical Easterly Jet during boreal summer. The boundaries of this region are adapted from the INDian Ocean EXperiment (INDOEX, Mitra, 2004) in order not to overlap other boxes. Finally we choose a fourth region over the Pacific Ocean and between the latitudes of 10°S and the equator, referred below as the Pacific warm pool region (WP) and characterised by SST up to 32 °C (Jauregui and Chen, 2023), favourable for deep convection.

Figures 10b and 10c show the typical wind speed profiles and wind shears for each region. While Houchi et al. (2010) performed a climatology of atmospheric horizontal wind and wind shear, they did not examine the typical wind profiles for different cloud regimes. On the other hand, some observational studies (Tian et al. 2021; Savazzi et al. 2022) analysed wind shears in different convective regimes, but their observations were concentrated in particular regions. Here, our results show at a global scale the wind profiles associated to different cloud regimes. The TrSc and Cu profiles exhibit an eastward acceleration from the surface to the core of the subtropical jet stream at about 12 km of altitude. The TrSc and Cu winds are both negative near the surface and change sign in the lower troposphere, at 3 km and 5 km for the TrSc and Cu regions, respectively. This is consistent with Helfer et al. (2020), who mention that the winds in trade-wind cumulus regions become increasingly eastward with height. The average wind profile observed over the Cu region is in good qualitative agreement with the averaged wind profile observed between the surface and 5 km of altitude during EUREC4A field campaign in January and February 2020, that targeted a shallow cumulus dominated area around Barbados (Savazzi et al., 2022). Within the altitude range of 1-12 km, the average wind shears in the TrSc and Cu regions are positive (Fig. 10b). Helfer et al. (2020) note that in the Cu region, the vertical shear in the zonal wind component is to first order set by large-scale meridional temperature gradients through the thermal wind relation, and therefore $\partial_z u > 0$ is typical for most of the year. The TrSc

region exhibits a stronger wind shear than the Cu region in the lower troposphere, which is consistent with the sharp transition of meteorological variables noted there by Hourdin et al. (2019). Over the Indian Ocean, we observe eastward (positive) winds between the surface and 14 km of altitude. Above 14 km of altitude, the wind speeds change direction and become westward. Below 10 km, the wind shear is positive but weak (lower than 10^{-3} s^{-1}). Above 10 km, the observed wind shears become negative, reaching -1.8×10^{-3} s^{-1} at 13 km of altitude because of the presence of the Tropical Easterly Jet just above (as also depicted in Fig. 7b). Above the warm pool, the wind is westward in the whole troposphere and the wind shears are weak, between -5×10^{-4} and 5×10^{-4} s^{-1} throughout the entire profile. Weak wind shears are explained by the presence of a strong convection in this region of high SST (Hibbert et al. 2023). Our result is consistent with the findings of Tian et al. (2021), who note that the wind shear in the mid-troposphere in a deep convective regime is significantly weaker than in situations dominated by lower convective clouds (below 7 km). This suggests an important role of wind shear in limiting the vertical extent of convection.
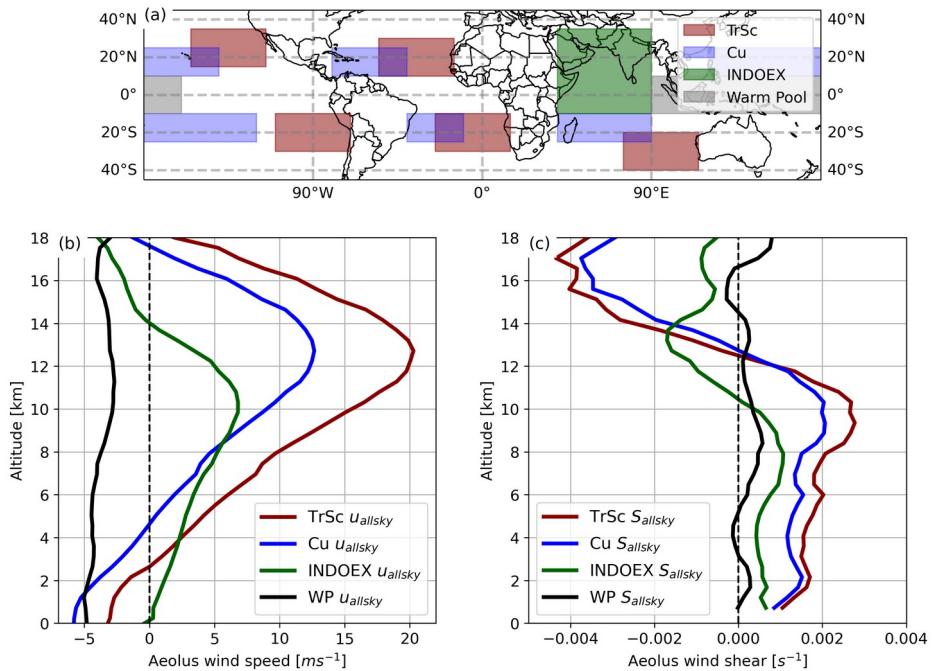
Figure 10: (a) map of the different regions considered. Average (b) wind speed profiles and (c) wind shear profiles retrieved in each region during the year 2020. The wind shear at each altitude z is defined as the difference between the wind two layers above z (960 m above z) and the wind two layers below z (960m under z).

To study the differences between the wind speeds within clouds and their surrounding clear sky, we identify for each region

930 profiles containing adjacent cloudy layers in the vertical direction and that are at least 2 km thick in total, typically associated to convective clouds (more details are given in Fig. B9). We record the cloudy wind speed observed in the uppermost cloudy layer (noted u_{cloud_up}) as well as its altitude, and the cloudy wind speed 2 km below the uppermost cloudy layer (noted u_{cloud_down}). We compute the wind shear between these two layers distant of 2 km (noted S_{cloud}). In the same orbit, among the surrounding profiles, we look for the closest profile located at a distance shorter than 100 km that exhibits clear

935 sky winds everywhere in this 2 km thick layer. We record the clear sky wind within this profile (noted $u_{clear\_surrounding\_cloud\_up}$) at the same altitude as the uppermost cloudy layer. We also record the clear sky wind speed (noted $u_{clear\_surrounding\_cloud\_down}$) 2 km under $u_{clear\_surrounding\_cloud\_up}$, coming from the same profile. We compute the clear sky wind shear in the surrounding of the cloud (noted $S_{clear\_surrounding\_cloud}$). Each cloud and its environment are therefore associated to a group of six variables including four wind speeds and two wind shears. A two-sided T-test is applied to test the significance of the differences in Fig. 11 and

940 is passed at each altitude level if the p-value < 0.05. ~~The random error is thus smaller than the typical horizontal wind speed difference between the uppermost cloudy layer $u_{cloud\_up}(z)$ and its clear sky surrounding $u_{clear\_surrounding\_cloud\_up}(z)$, which was estimated to 3 ms^{-1} in the airborne case study (Fig. 9) and documented to be several ms^{-1} generally.~~

Figure 11a shows the average profile of $u_{cloud\_up}(z)$ and the average profile of $u_{clear\_surrounding\_cloud\_up}(z)$ for the different regions.

945 Because of the smaller vertical extent of low clouds, and particularly boundary layer clouds (Wood et al., 2012; Cesana et al., 2019) which typically do not exceed 1 km, and because of the stronger attenuation of low liquid clouds (Guzman et al., 2017), there are no occurrences of Aeolus wind shears calculated over 2 km vertically below 5 km of altitude (Fig. B6). We find that for both TrSc and Cu, between 5 and 10 km of altitude, $u_{cloud\_up}(z)$ is eastward and 1 to 3 ms^{-1} slower (statistically significant) than its paired $u_{clear\_surrounding\_cloud\_up}(z)$ at the same altitude. We also note that at these altitudes the average wind

950 shear within the cloud $S_{cloud}(z)$ is always lower than 10^{-3} s^{-1}, while the one observed in the clear sky surrounding the cloud is positive and ranges between 10^{-3} and 3.5×10^{-3} s^{-1}. In contrast, at altitudes higher than 14 km where the clear sky wind shear is negative, $u_{cloud\_up}(z)$ is significantly more eastward than its paired $u_{clear\_surrounding\_cloud\_up}(z)$, and the differences range from 1 to 2 ms^{-1}. We thus emphasise that over the stratocumulus and cumulus dominated regions, the wind shear within clouds is systematically smaller than the wind shear in the clear sky surrounding the clouds, and this difference is statistically

955 significant. In addition, over these two regions, the differences between $u_{cloud\_up}(z)$ and $u_{clear\_surrounding\_cloud\_up}(z)$ can reach above 3 ms^{-1}, particularly at altitudes where the wind shear $S_{clear\_surrounding\_cloud}(z)$ is the largest. Over the Pacific warm pool, $u_{clear\_surrounding\_cloud\_up}(z)$ and $u_{cloud\_up}(z)$ are both westward between 14 and 16 km of altitude, which correspond to deep convective CTH in this region (Sassen et al., 2009). Within this altitude range, $u_{clear\_surrounding\_cloud\_up}(z)$ is 1 to 2 ms^{-1} faster than $u_{cloud\_up}(z)$. $S_{clear\_surrounding\_cloud}(z)$ ranges between -1.5×10^{-3} and -2.5×10^{-3} s^{-1}. Tian et al., (2021) reported

960 similar wind shears in the upper troposphere around deep convective clouds over the Amazon. $S_{clear\_surrounding\_cloud}(z)$ is 10^{-3} s^{-1} larger (in absolute value) than $S_{cloud}(z)$.

965

980
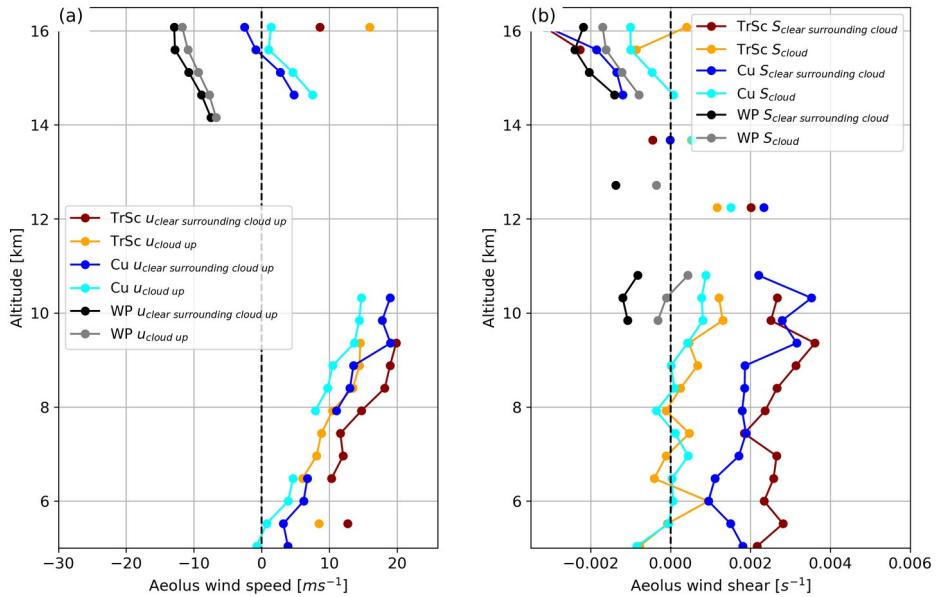
Figure 11~~10~~: (a) average wind speed profiles retrieved within the uppermost cloudy layer $u_{cloud\ up}(z)$ and average of the closest clear sky wind speed $u_{clear\ surrounding\ cloud\ up}(z)$ observed by over each region during the year 2020. Only values where $u_{cloud\ up}(z)$ and $u_{clear\ surrounding\ cloud\ up}(z)$ are significantly different (two sided T-test with p-value < 0.05) are plotted. (b) average wind shear profiles, defined at each altitude z as the difference between the wind two layers above z (960 m above z) and the wind two layers below z (960m under z).

985

4.3.3 First validation of K-theory for wind in the free troposphere with Aeolus

We observe for the first time from space a systematic anti-correlation between the sign of the $u_{cloud\_up}(z)$ − $u_{clear\_surrounding\_cloud\_up}(z)$ and the sign of the wind shear in the surroundings of clouds, $S_{clear\_surrounding\_cloud}(z)$, at each altitude. In fact, the differences $u_{cloud\_up}(z)$ − $u_{clear\_surrounding\_cloud\_up}(z)$ show a quasi linear relationship (Fig. 12) with the values of $S_{clear\_surrounding\_cloud}(z)$ for the TrSc, Cu and the INDOEX regions with correlation coefficients of respectively R=-0.87, R=-0.94

and R=-0.8. Our results are very consistent with those obtained with a Cloud Resolving Model by Grubisic and Moncrieff (2000), who also show a weaker horizontal wind in the updraft (analogous to our cloudy sky) than in the downdraft region (analogous to the clear sky surrounding the cloud) in positive wind shear conditions, and a larger difference between updraft and downdraft winds when the wind shear increases. This result suggests that for strongly sheared regions, Aeolus, at its coarse resolution can observe significant differences between the winds in the uppermost layer of convective clouds and their clear sky surrounding, and these differences anti-correlate well with the wind shear in the surrounding of clouds. This is in line with the K-theory, that stipulates that the averaged wind perturbations in a turbulent fluid are proportional to the averaged wind shears. Over the Pacific warm pool and the INDOEX region, as expected, the wind profiles are overall less sheared than over TrSc and Cu regions, with differences between $u_{cloud\_up}(z)$ and $u_{clear\_surrounding\_cloud\_up}(z)$ below 2 ms^{-1}.
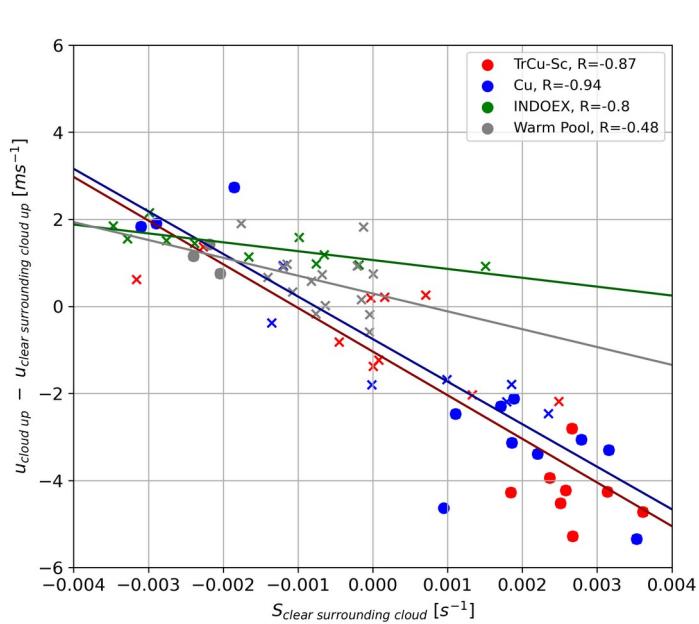
Figure 12~~11~~: Scatter plot of the wind shear in the clear sky surrounding the cloud $S_{clear\_surrounding\_cloud}(z)$ **and the wind speed perturbation associated to the presence of a cloud,** $u_{cloud}(z) - u_{clear\_surrounding\_cloud}(z)$ **for each region. Each point represents an altitude level. We used circles to denote altitudes where both** $u_{cloud}(z) - u_{clear\_surrounding\_cloud}(z)$ **and** $S_{cloud}(z) - S_{clear\_surrounding\_cloud}(z)$ **significantly different (two sided T-test with p-values < 0.05) and crosses otherwise.**

5 Summary and future work

The observations presented in this paper display for the first time merged cloud vertical profiles and vertical profiles of horizontal wind at global-scale. We constructed cloud profiles at 3 km of horizontal resolution and re-sampled vertically at 480 m, using Aeolus L1A uncalibrated backscatter data coming from the detector of the Mie channel only. Corrections were applied to compensate for the varying vertical resolution and optical properties of the detector, the lack of the cross-polar backscattered signal as well as the increasing number of hot pixels during the mission. Globally, the obtained cloud fraction profiles showed a good agreement with CALIPSO-GOCCP cloud profiles with an R^2 of 0.84~~79~~, Pearson correlation of 0.92~~86~~ and local cloud fraction differences below 2.5~~3~~ % in most of the entire free troposphere. Using this cloud detection, we re-sampled the already calibrated and validated L2B Aeolus winds on a curtain of 3 km of horizontal resolution and 480 m of vertical resolution. We assessed that Aeolus re-sampled clear sky winds at 3 km are representative of the actual wind at 3 km of resolution, (with differences below 1 ms^{-1} in 78~~84~~% of the cases), based on airborne Doppler Wind Lidar data and a regional weather model simulation at high spatial resolution.

To highlight the potential of this dataset, we showed unique global, perfectly co-located, direct observations of cloud and wind profiles within the entire troposphere during boreal summer 2020. Unsurprisingly, the main zonal global-scale circulations are well captured by Aeolus. This includes the almost cloud-free subtropical and tropical jet streams as well as the tropical tropopause circulation. This opens perspectives of exploring deeper the shift in intensity and position of the subtropical jet stream induced by the cloud radiative effect, particularly in regions with a low number of in-situ observations. ~~We also found that over the Northern Atlantic and Pacific Oceans, regions with the strongest wind shears between 2 and 10 km of altitude (> 3x10^{-3} s^{-1}) are the less cloudy at 10 km of altitude (cloud fraction < 2 %).~~ Over the Indian Ocean, we observed low altitude cloud fractions of about 30 % in January that decrease until April 2020 and then increase again while the Monsoon onsets (June to September 2020). In the upper troposphere, when the Tropical Easterly Jet starts (early June), winds in its core quickly reach speeds of above 40 ms^{-1} and high cloud fractions suddenly increase at the same time, exceeding 30 %.

Finally, regarding circulations at cloud scales inferior to 100 km, we analysed the averaged wind speed differences between the uppermost layer of convective clouds and the surrounding clear sky. After confirming that these wind speed differences can be observed at the resolution of Aeolus observations (using an airborne case study averaged at the resolution of Aeolus), we split the study in regions having different large scale circulations. Over regions dominated by Stratocumulus and Cumulus clouds, convective motions induce large wind speed differences between the uppermost cloudy layer and their clear sky environment, exceeding 3 ms^{-1} at some altitudes. We finally showed that these wind speed differences anti-correlate with the wind shear in the clear sky surrounding the cloud. This anti-correlation is particularly strong with R=-0.94~~0.93~~ over

Cumulus and R=-0.87~~0.89~~ over Stratocumulus dominated regions. This is a direct evidence that horizontal momentum transported by convective motions can be observed by Aeolus.

These few applications show the potential of this new observations for studying wind-cloud interactions at different horizontal scales, extending from 3 km to the global scale. In the near future we plan to focus on the correlation between cirrus covers and the strengthening of horizontal winds (Das et al., 2011), and on the interactions between the cloud radiative effect and jet stream shifting (Voigt et al., 2021). The case study on the tropical cyclone also opens perspectives to study how the wind shear contributes in the organization of shallow convection from random patterns to clusters (Mieslinger et al., 2019 ; Bony et al., 2020) and sometimes mesoscale convective systems (Houze 2004 ; Schumacher and Rasmussen, 2020 ; Abramian et al., 2022).

Appendix A: Complements relative to cloud detection
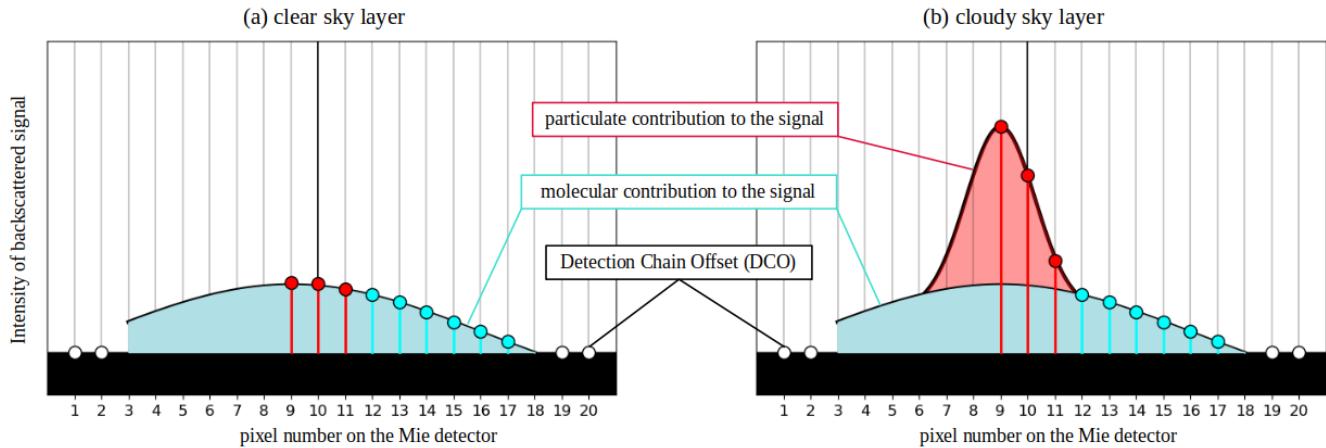
Figure A1. Schematics of the signal received on the detector of the Mie channel (a) in the case of a clear sky layer and (b) in the case of a cloudy layer. Note that these are not at scale and in the case of a cloudy scene, the particulate backscattered signal peak is much larger compared to the molecular backscattered spectrum.

On Fig. A1, we display the intensity of the backscattered signal retrieved on each of the 16 central pixels (pixels 3-16) of the Mie channel detector in a single profile at one altitude level. Note that the pixels 1, 2, 19 and 20 only store information about the Detection Chain Offset (DCO), and the average value stored on these four pixels is averaged and subtracted to the backscattered signal. In the case of Aeolus, a fraction of the molecular backscattered signal is retrieved on the Mie detector and shown in blue. The intensity of this molecular signal essentially depends on the molecular density. The centre~~center~~ of the distribution, contains information about both the molecular and particulate backscattered signals. The red part is only due to the presence of aerosols such as cloud droplets or ice particles which are much slower than individual molecules. Therefore, the intensity of the red peak at the center increases in the presence of a cloud as shown in Fig. A1b and is nonexistent or small in the absence of clouds as shown in Fig. A1a.

In the case of Fig. A1, the signal retrieved in the pixels corresponding to the peak of the backscattered signal is found on pixel 9 (left part of the Mie channel detector), therefore the value of the signal stored in pixel 9 and in the two neighboring pixels on its right (pixels 10 and 11) are summed and noted $I_{part}(z_{L1A})$ in this paper, z_{L1A} being the altitude of the center of a layer in a L1A profile. The signal retrieved in the six following pixels to the right of pixel 11 (pixels 12-17) are summed and correspond to the molecular backscatter, called $I_{mol}(z_{L1A})$. Although the molecular backscattered signal (in arbitrary unit) in this approach does not represent the actual molecular backscatter (in m^{-1} sr^{-1}), it is proportional to it, enabling us to use the difference ~~between~~ $I_{part}(z_{L1A})$ ~~and~~ $I_{mol}(z_{L1A})$ to determine the cloud mask.
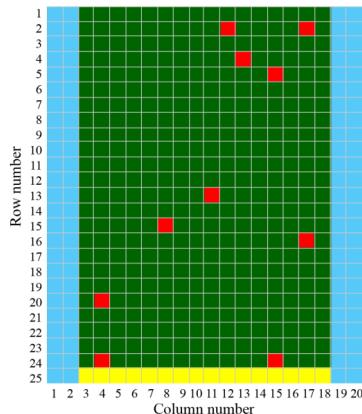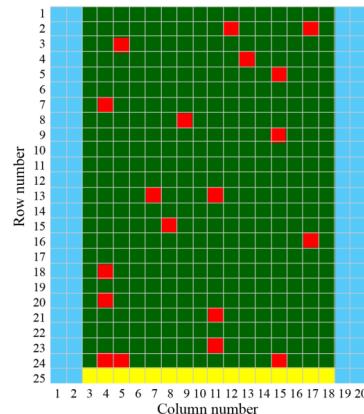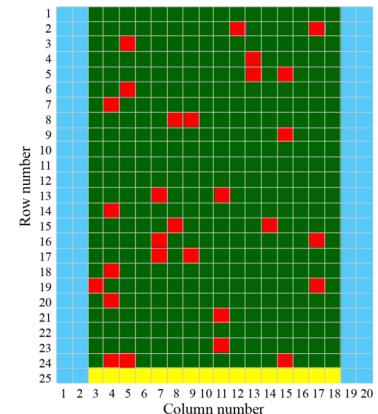
Figure A2. Hot pixel maps corresponding to (a) 14 June 2020 (compare with Weiler et al., 2021), (b) 31 December 2020 (end of our study) and 1 July 2023 (end of Aeolus mission). Hot pixels are identified by comparing each detector pixel value against its immediate neighbors within the same Mie detector row: pixels exceeding all neighboring values are flagged and counted across all daily orbits. The resulting frequency maps are normalized by their maximum count and thresholded at 0.2, with pixels above this empirical threshold marked as "hot".

For our study, we used the hot pixel map of 31 December 2020 (Fig. A2b) but follow-on study based on a longer period may use the most conservative hot pixel map of 1 July 2023 (Fig. A2c).
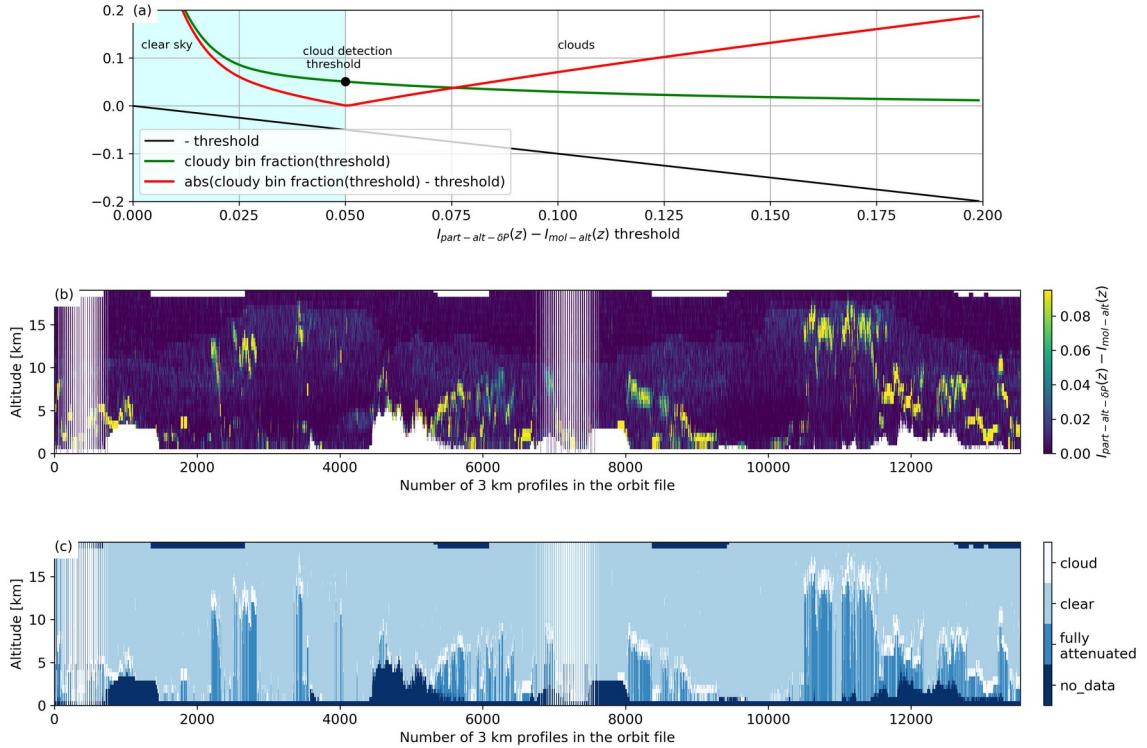
Figure A3. (a) Fraction of cloudy bins retrieved depending on the applied cloud detection threshold (green curve) and cloud detection threshold (black dot) for the orbit 2020-09-12T09–2020-09-12T11 (same as Fig. 5). (b) Cross section of $I_{part-alt-\delta P}(z) - I_{mol-alt}(z)$ for the same orbit and (c) the resulting cloud mask.

For each profile, a layer is declared cloudy when and $I_{part-alt-\delta P}(z) - I_{mol-alt}(z)$ exceeds a certain threshold. We found that from an orbit to the other, the distributions of particulate and molecular backscatters fluctuate. We suggest that a good way to find the cloud detection threshold on $I_{part-alt-\delta P}(z) - I_{mol-alt}(z)$ for each orbit, is to compute the fraction of cloudy bins obtained for various thresholds on $I_{part-alt-\delta P}(z) - I_{mol-alt}(z)$, ranging from 0.01 to 0.20 (arbitrary units). The fraction of cloudy bins decreases quickly for low values of $I_{part-alt-\delta P}(z) - I_{mol-alt}(z)$, which correspond to the clear sky and Poisson-distributed noise. It then decreases slowly, for larger particulate backscatters associated with clouds. The cloud detection threshold (named thresh$_1$) is found when abs(cloudy bin fraction(threshold) – threshold) is minimum. Note that the determination of the cloud detection threshold is evaluated while accumulating all altitudes between the surface and 18 km of altitude. Therefore, this threshold is strongly weighted by the values of $I_{part-alt-\delta P}(z) - I_{mol-alt}(z)$ in the free troposphere, mostly free of Saharan dusts and aerosols, but containing a lot of clouds with larger $I_{part-alt-\delta P}(z) - I_{mol-alt}(z)$. Therefore, aerosol layers are classified as clear sky.

Figure A4 shows the map of low and mid-level clouds during the season where the most of Saharan dusts are observed. Overall, on the West coast of Africa at around 20° of latitude, the Aeolus cloud cover is approximately 10 % lower than CALIPSO-GOCCP below 8 km of altitude. CALIPSO-GOCCP cloud detection threshold was already restrictive enough to flag Saharan dusts as clear sky. Therefore, Saharan dusts are even less likely to be flagged as clouds in our Aeolus dataset.
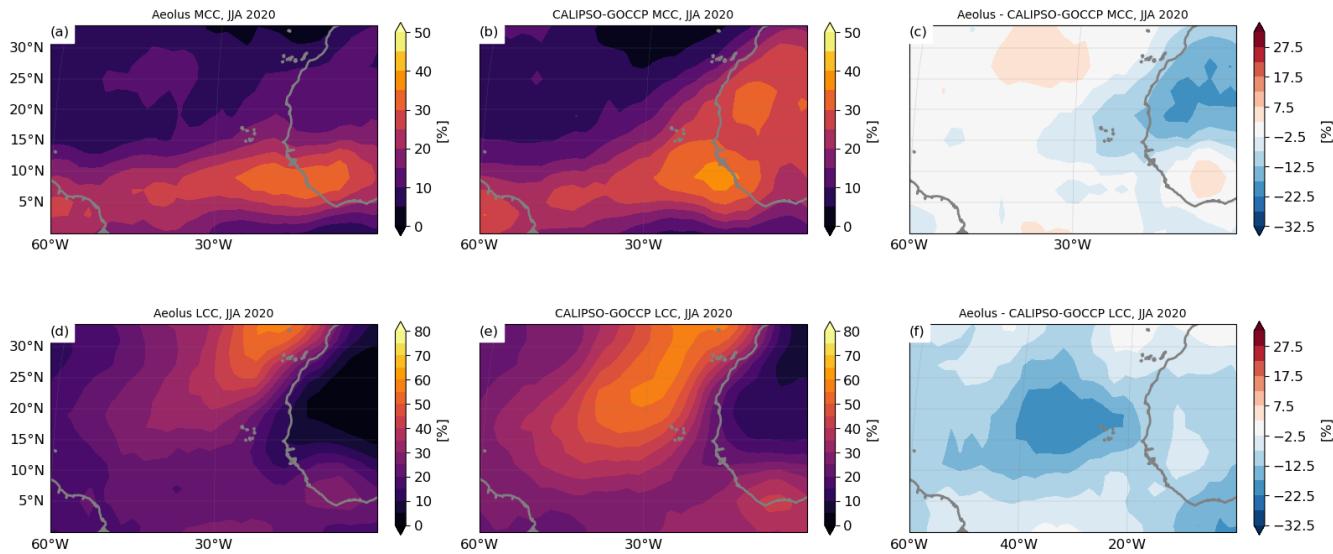
Figure A4. Maps of mid-level (4-8 km) cloud cover (a) Aeolus dataset (b) CALIPSO-GOCCP and (c) the difference Aeolus – CALIPSO-GOCCP for the year 2020. (d), (e) and (f) are the same but for low level clouds (0-4 km).

Appendix B: Complements relative to the dynamic variables estimates
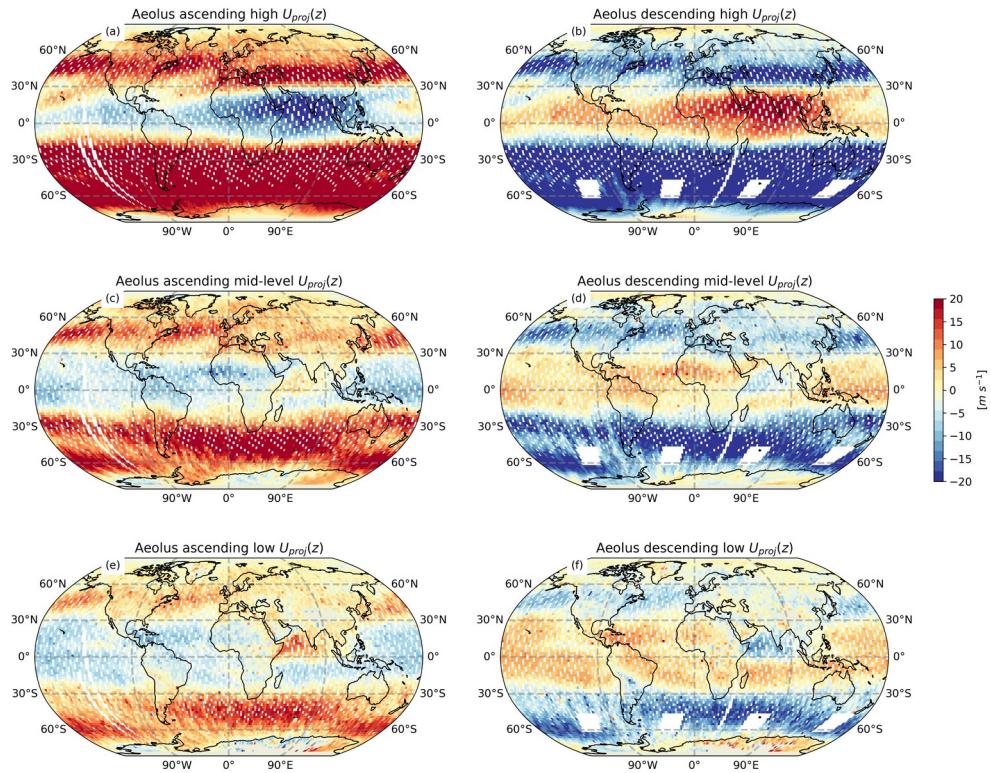
Figure B1: Global maps of Aeolus all-sky winds (a) above 6.5 km, (c) between 3.2 and 6.5 km, (e) between the surface and 3.2 km for 1800 LT ascending orbits between Jun–Aug 2020. (b), (d) and (f) are the same but for 0600 LT descending orbits., note how the winds for ascending orbits resemble to zonal winds while

Figure B1 illustrates that winds observed during ascending and descending orbits are nearly opposite and a change in the sign of the descending wind gives a good approximation of the zonal wind, especially within the latitude range 60°S-60°N. Indeed, differences exist between the wind observed at 0600 LT and 1800 LT and can be explained~~explain~~ by a diurnal contrast~~cycle~~ of the wind and slight differences in the laser pointing direction (~~line-of-sight,~~ Fig. 1). It is possible to estimate zonal and meridional winds from Aeolus but these require making hypothesis about the wind direction or averaging successive ascending and descending orbits. Zonal wind retrievals are detailed in Krisch et al., 2022.

Figure B2: Distribution of the differences between colocated, resampled, Mie winds retrieved in cloudy sky and Rayleigh winds that were substituted. Based on all bins during JJA 2020.

Figure B3: Same as Fig. 4 but all altitudes between the surface and 19 km are included for WRF (about 4000 independent segments of 87 km x 480 m).
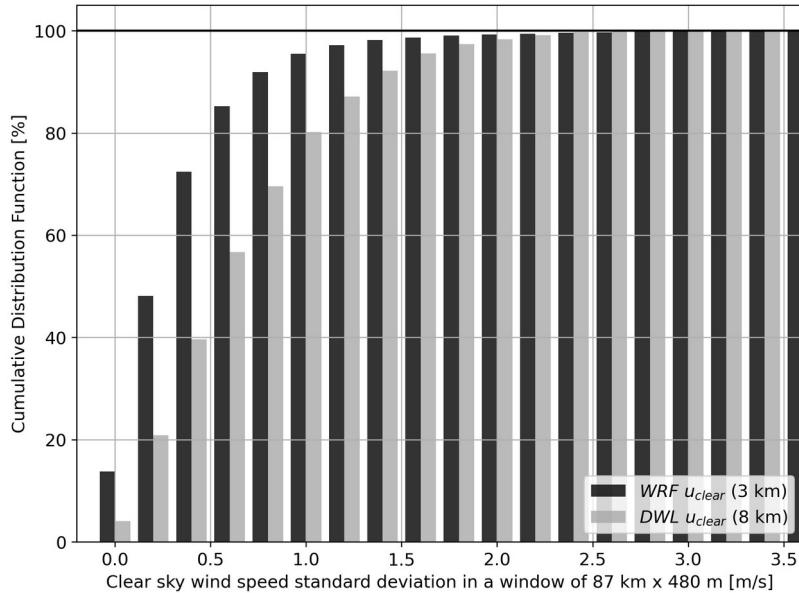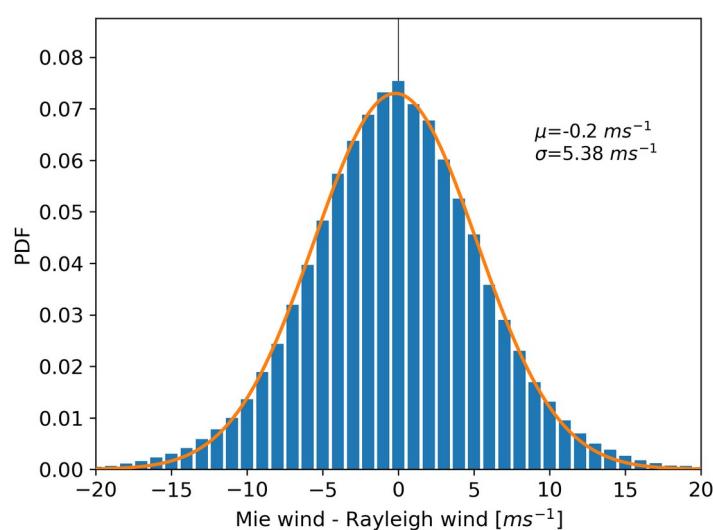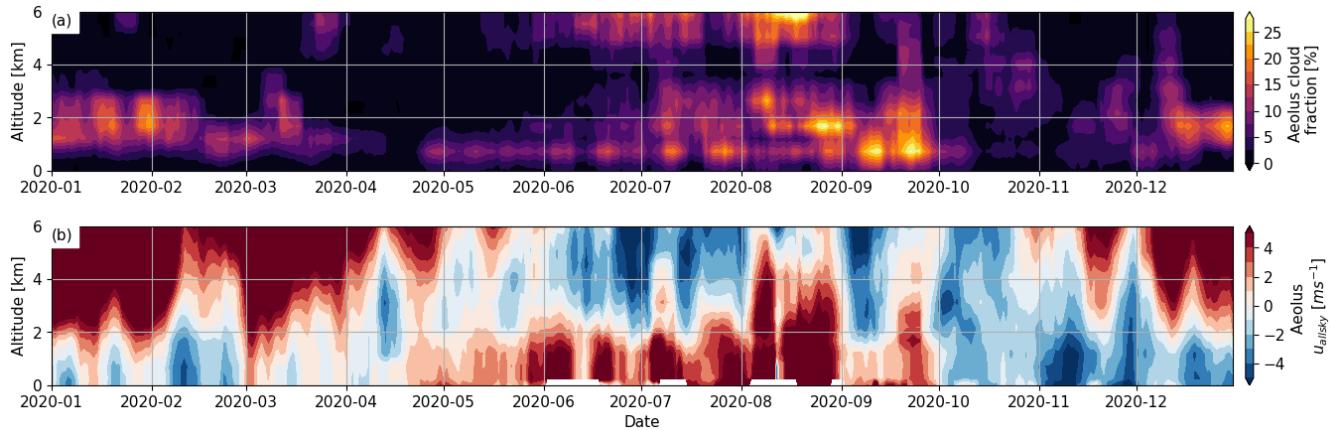
1240   **Figure B4 : Time series of (a) the average profiles of cloud fraction and (b) the average profiles of all-sky wind speed within (12°N-24°N, 55°E-75°E). A 7-day rolling mean is applied to see the typical direction of the wind and vertical cloud extent**
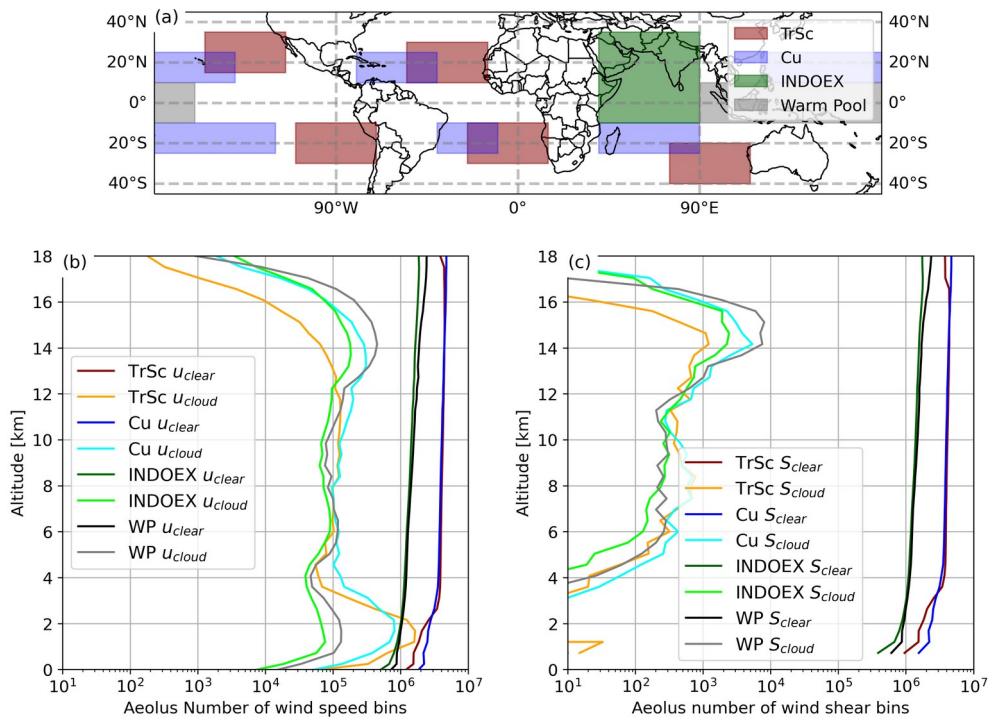
1265   **Figure B5: Map of the different regions for wind speed and wind shear differences. Stratocumulus transitioning (red) Cumulus (blue), INDOEX (green) and Pacific warm pool (black). Occurrences of (b) wind speed and (c) wind shear observations.**
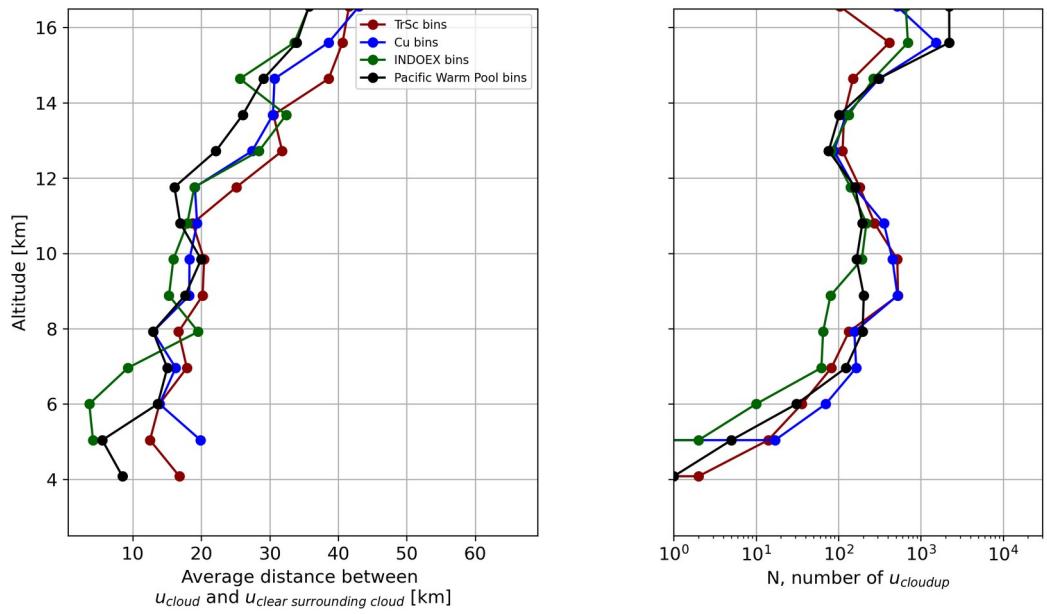
Figure B6: Average distance between pairs of $u_{cloud}(z)$ and $u_{clear\_surrounding\_cloud}(z)$. All pairs separated by a distance of over 100 km were discarded. (b) Occurrences of pairs at each altitude level.
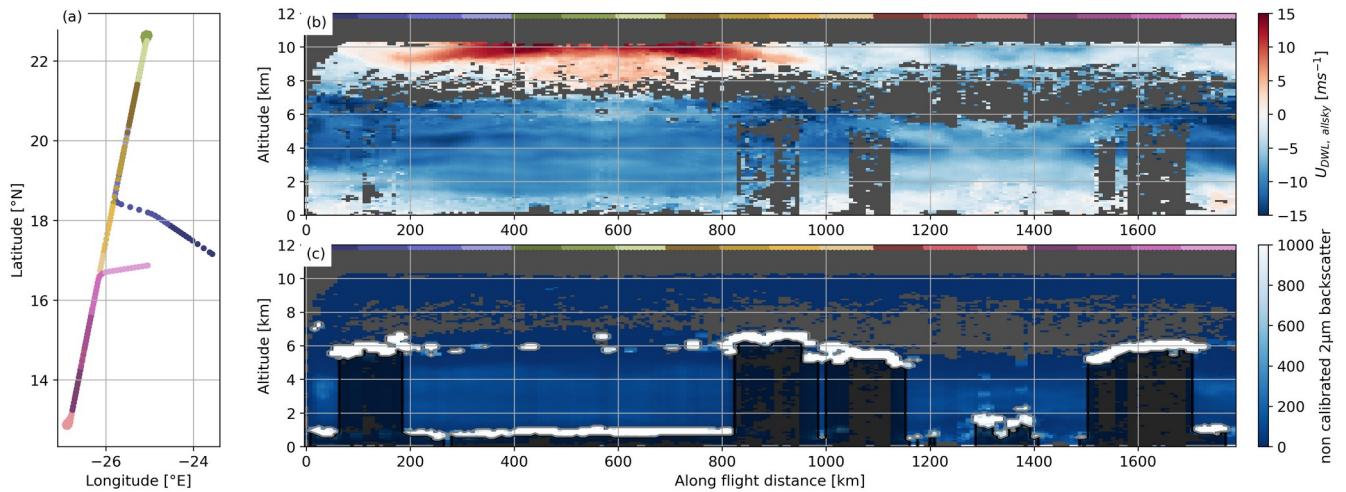
Figure B7: (a) position of airborne LIDAR profiles during AVATAR-T Flight (2021-09-08, same as Fig. 9) over Cape Verde **(b)** horizontal wind projected along Aeolus line-of-sight ($u_{DWL, allsky}$) at a horizontal resolution of 8 km and vertical resolution of 100 m. and **(c)** uncalibrated 2μm backscatter with clouds contoured (grey) and the sub-cloud layers shaded (black). We estimated that uncalibrated 2μm backscatter exceeding 500 is associated with clouds.
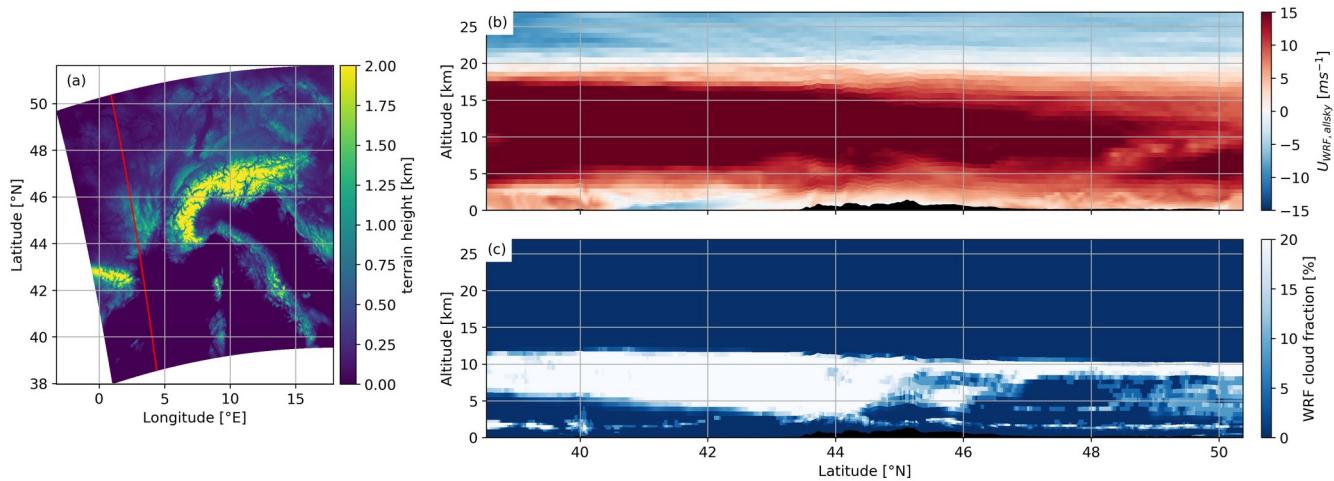
Figure B8: (a) terrain height of WRF simulation, the red curve corresponds to a theoretical orbit track of Aeolus. **(b)** Horizontal wind projected along Aeolus line-of-sight ($u_{WRF, allsky}$) at a horizontal resolution of 3 km and **(c)** the corresponding cloud fraction.
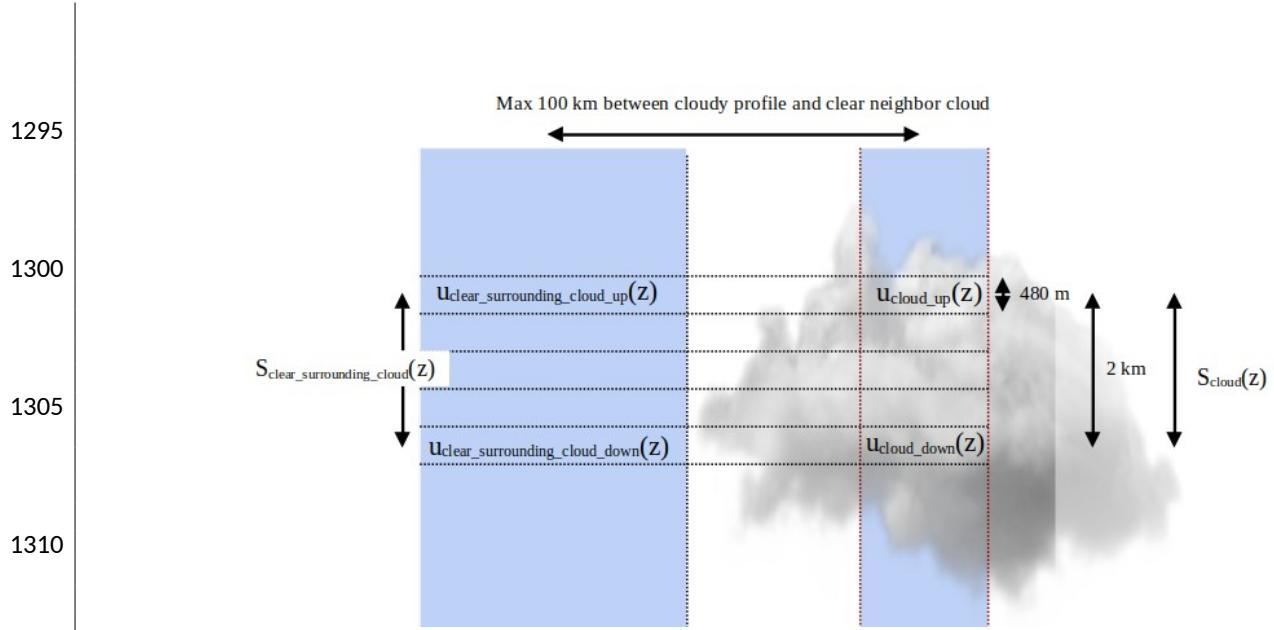
Figure B9: (a) complements relative to the calculations of wind shear within the cloud $S_{cloud}(z)$ and the surrounding clear sky wind shear $S_{clear\_surrounding\_cloud}(z)$

Data availability. ALADIN/Aeolus orbit files and gridded data presented in this paper are available via AERIS (https://dx.doi.org/10.25326/746). They are built from Aeolus Level 1A and Level 2B observations that can be accessed via the ESA Aeolus Online Dissemination System (https://aeolus-ds.eo.esa.int/oads/access/). CALIPSO-GOCCP version 3.1.4 (Chepfer et al., 2010) and ERA5 reanalyses (Hersbach et al., 2020) were accessible via Mesocentre ESPRI/IPSL.

Author contributions. ZT, MB and HC drafted the article. The Aeolus dataset development was performed by ZT and AGF. The data analysis was performed by ZT, MB, and HC. The WRF simulation was performed by SB and the airborne lidar data were collected by BW. All authors were involved in the writing and investigation.

Competing interests. The authors declare that they have no conflict of interest.

Acknowledgments. The authors thank Mesocentre ESPRI/IPSL for the computation resources. We also thank ESA dissemination team for the access to Aeolus data and AERIS for the storage of the dataset. We thank Dr. Louise Nuijens for the interesting discussions regarding convective momentum transport that participated to the motivations of this study. The authors thank the people involved in the production of the WRF simulation, performed on the HPC resources of TGCC under the allocations A0050106877 and A0070106877 made by GENCI. The authors also thank the DLR for the deployment of the Falcon and 2µm Doppler Wind Lidar during AVATAR-T campaign. We deeply thank the two anonymous reviewers for their great inputs, which helped to improve a lot the manuscript.

Financial support. This research was supported by European Space Agency and European Aeronautic Defence and Space company (EADS) in the framework of ZT's PhD.

References

Abramian, S., Muller, C. and Risi, C.: Shear-Convection Interactions and Orientation of Tropical Squall Lines, Geophysical Research Letters, 49, https://doi.org/10.1029/2021GL095184 , 2022.

Aeolus Data Innovation and Science Cluster (Aeolus DISC) : The Earth Explorer Mission Aeolus for atmospheric wind observations – Final Report from the Aeolus Data Innovation and Science Cluster DISC of Phase E, https://doi.org/10.57676/93c3-n766 , 2024.

Ali, S., Mehta, S. K., Ananthavel, A., and Reddy, T. V. R.: Temporal and vertical distributions of the occurrence of cirrus clouds over a coastal station in the Indian monsoon region, Atmos. Chem. Phys., 22, 8321–8342, https://doi.org/10.5194/acp-22-8321-2022 , 2022.

Baars, H., Herzog, A., Heese, B., Ohneiser, K., Hanbuch, K., Hofer, J., Yin, Z., Engelmann, R., and Wandinger, U.: Validation of Aeolus wind products above the Atlantic Ocean, Atmos. Meas. Tech., 13, 6007–6024, https://doi.org/10.5194/amt13-6007-2020 , 2020.

Ban, N., Caillaud, C., Coppola, E., Pichelli, E., Sobolowski, S., Adinolfi, M., Ahrens, B., Alias, A., Anders, I., Bastin, S. et al.: The first multi-model ensemble of regional climate simulations at the kilometer-scale resolution, Part I: Evaluation of precipitation. *Clim. Dyn. 57, 275-302*, https://doi.org/10.1007/s00382-021-05708-w , 2021

Belova, E., Kirkwood, S., Voelger, P., Chatterjee, S., Satheesan, K., Hagelin, S., Lindskog, M., Körnich, H.: Validation of Aeolus winds using ground-based radars in Antarctica and in northern Sweden, Atmospheric Measurement Techniques, 14, 5415–5428, https://doi.org/10.1007/978-3-031-53618-2_6 , 2021.

Bernardino, M., Rusu, L., & Soares, C. G.: Evaluation of the wave energy resources in the Cape Verde Islands. *Renewable Energy, 101,* 316-326, https://doi.org/10.1016/j.renene.2016.08.040 , 2017

Bodas-Salcedo, A., Webb, M. J., Bony, S., Chepfer, H., Dufresne, J. L., Klein, S. A., ... & John, V. O.: COSP: Satellite simulation software for model assessment. *Bulletin of the American Meteorological Society*, *92*(8), 1023-1043, https://doi.org/10.1175/2011BAMS2856.1 , 2011

Bony, S., Schulz, H., Vial, J., & Stevens, B.: Sugar, Gravel, Fish, and Flowers: Dependence of Mesoscale Patterns of Trade-Wind Clouds on Environmental Conditions, Geophysical Research Letters, 48, https://doi.org/10.1029/2019GL085988 , 2020.

Brueck, M., Nuijens, L. and Stevens, B.: On the Seasonal and Synoptic Time-Scale Variability of the North Atlantic Trade Wind Region and Its Low-Level Clouds, American Meteorological Society, 72, 1428-1446, https://doi.org/10.1175/JAS-D-14-0054.1 , 2015.

Cesana, G., Del Genio, A. D., and Chepfer, H.: The Cumulus And Stratocumulus CloudSat-CALIPSO Dataset (CASCCAD), Earth Syst. Sci. Data, 11, 1745–1764, https://doi.org/10.5194/essd-11-1745-2019 , 2019.

Chepfer, H., Bony, S., Winker, D., Cesana, G., Dufresne, J. L., Minnis, P., Stubenrauch, C. J. and Zeng, S.: The GCM-Oriented CALIPSO Cloud Product (CALIPSO-GOCCP), Journal of Geophysical Research, 115, D00H16, https://doi.org/10.1029/2009JD012251 , 2010.

Chepfer, H., Cesana, G., Winker, D., Getzewich, B., Vaughan, M. and Liu, Z.: Comparison of Two Different Cloud Climatologies Derived from CALIOP-Attenuated Backscattered Measurements (Level 1): The CALIPSO-ST and the CALIPSO-GOCCP, American Meteorological Society, 30, 725–744, https://doi.org/10.1175/JTECH-D-12-00057.1 , 2013.

Chepfer, H., Brogniez, H. and Noel, V.: Diurnal variations of cloud and relative humidity profiles across the tropics, Nature Scientific Report, 9, https://doi.org/10.1038/s41598-019-52437-6 , 2019.

Dabas, A., Ehlers, F., Flament, T., Trapon, D., Lacour, A., et al.: Optimization of Aeolus' aerosol optical properties by maximum-likelihood estimation. Atmos. Meas. Tech., 15, 185–203. https://doi.org/10.5194/amt-15-185-2022 , 2022.

Das, S.K., Chiang, C-W., and Nee, J-B. : Influence of tropical easterly jet on upper tropical cirrus: An observational study from CALIPSO, Aura-MLS, and NCEP/NCAR data, Journal of Geophysical Research, 116, https://doi.org/10.1029/2011JD015923 , 2011.

Donovan, D. P., van Zadelhoff, G.-J., and Wang, P.: The EarthCARE lidar cloud and aerosol profile processor (A-PRO): the A-AER, A-EBD, A-TC, and A-ICE products, Atmos. Meas. Tech., 17, 5301–5340, https://doi.org/10.5194/amt-17-5301-2024 , 2024a.

Donovan, D. P., van Zadelhoff, G.-J., and Wang, P.: Aeolus/ALADIN Algorithm Theoretical Basis Document Level 2A products AEL-FM, AEL-PRO, Document Version V2.00, https://earth.esa.int/documents/d/earth-online/aeolus-level-2a-algorithm-theoretical-baseline-document-ael-fm-and-ael-pro-products , 2024b.

Feofilov, A. G. and Stubenrauch, C. J.: Diurnal variation of high-level clouds from the synergy of AIRS and IASI space-borne infrared sounders, Atmos. Chem. Phys., 19, 13957–13972, https://doi.org/10.5194/acp-19-13957-2019 , 2019.

Feofilov, A. G.: Interactive comment on "Characterization of dark current signal measurements of the ACCDs used on-board the Aeolus satellite" by Fabian Weiler et al., Atmos. Meas. Tech. Discuss., https://doi:10.5194/amt-2020-458-RC1 , 2021.

Feofilov, A. G., Chepfer, H., Noël, V., Guzman, R., Gindre, C., Ma, P.-L., and Chiriaco, M.: Comparison of scattering ratio profiles retrieved from ALADIN/Aeolus and CALIOP/CALIPSO observations and preliminary estimates of cloud fraction profiles, Atmos. Meas. Tech., 15, 1055–1074, https://doi.org/10.5194/amt-15-1055-2022 , 2022.

Flamant, P., Cuesta, J., Denneulin, M.-L., Dabas, A., and Huber, D.: ADM-Aeolus retrieval algorithms for aerosol and cloud products, Tellus A, 60, 273–288, https://doi.org/10.1111/j.1600-0870.2007.00287.x , 2008.

Fujiwara, M., Xie, S.-P., Shiotani, M., Hashizume, H. and Hasebe, F.: Upper-tropospheric inversion and easterly jet in the tropics, Journal of Geophysical Research, 108, https://doi.org/10.1029/2003JD003928 , 2003.

Goldberg, R. A., Feofilov, A. G., Pesnell, W. D., and Kutepov, A. A.: Inter-hemispheric Coupling during Northern Polar Summer Periods of 2002–2010 using TIMED/SABER Measurements, J. Atmos. Sol.-Terr. Phys., 104, 277–284, https://doi.org/10.1016/j.jastp.2012.11.018 , 2013.

Grubisic, V. and Moncrieff, M.W.: Parameterization of Convective Momentum Transport in Highly Baroclinic Conditions, Journal of the Atmospheric Sciences, 57, 3035–3049, https://doi.org/10.1175/1520-0469(2000)057<3035:POCMTI>2.0.CO;2 , 2000.

Guzman, R., Chepfer, H., Noel, V., Vaillant de Guélis, T., Kay, J. E., Raberanto, P., Cesana, G., Vaughan, M. A. and Winker D. M.: Direct atmosphere opacity observations from CALIPSO provide new constraints on cloud-radiation interactions, J. Geophys. Res. Atmos., 122, 1066–1085, https://doi.org/10.1002/2016JD025946 , 2017

Helfer, K. C., Nuijens, L., de Roode, S. R., and Siebesma, A. P.: How wind shear affects trade-wind cumulus convection. Journal of Advances in Modeling Earth Systems, 12, e2020MS002183. https://doi.org/10.1029/2020MS002183 , 2020.

Hemanth Kumar, A., Venkat Ratnam, M., Sunilkumar, S.V., Parameswaran, K. and Krishna Murthy, B.V.: Role of deep convection on the tropical tropopause characteristics at sub-daily scales over the South India monsoon region, Atmos. Res., 14–24, https://doi.org/10.1016/j.atmosres.2015.03.012 , 2015.

Hersbach, H., Bell, B., Berrisford, P., Hirahara, S., Horányi, A., Muñoz-Sabater, J., Nicolas, J., Peubey, C., Radu, R., Schepers, D., Simmons, A., Soci, C., Abdalla, S., Abellan, X., Balsamo, G., Bechtold, P., Biavati, G., Bidlot, J., Bonavita, M., Chiara, G., Dahlgren, P., Dee, D., Diamantakis, M., Dragani, R., Flemming, J., Forbes, R., Fuentes, M., Geer, A., Haimberger, L., Healy, S., Hogan, R. J., Hólm, E., Janisková, M., Keeley, S., Laloyaux, P., Lopez, P., Lupu, C., Radnoti, G., Rosnay, P., Rozum, I., Vamborg, F., Villaume, S., and Thépaut, J. N.: The ERA5 global reanalysis. Q. J. Roy. Meteor. Soc., 146, 1999–2049, https://doi.org/10.1002/qj.3803 , 2020.

Hibbert, K., Glenn, E., Smith, T. M., & González-Cruz, J. E.: Changes to sea surface temperatures and vertical wind shear and their influence on tropical cyclone activity in the Caribbean and the main developing region. *Atmosphere*, *14*(6), 999, https://doi.org/10.3390/atmos14060999 , 2023

Hierro, R., Steiner, A. K., de la Torre, A., Alexander, P., Llamedo, P., & Cremades, P.: Orographic and convective gravity waves above the Alps and Andes Mountains during GPS radio occultation events–a case study. *Atmospheric Measurement Techniques*, *11*(6), 3523-3539, https://doi.org/10.5194/amt-11-3523-2018 , 2018

Hildebrand, P. H.: Shear-Parallel Moist Convection over the Tropical Ocean: A Case Study from 18 February 1993 TOGA COARE. Mon. Weather Rev., 126(7), 1952–1976. https://doi.org/10.1175/1520-0493(1998)126<1952:spmcot>2.0.co;2 , 1998.

Höjgård-Olsen, E., Chepfer, H., &Brogniez, H.: Satellite observed sensitivity of tropical clouds and moisture to sea surface temperature on various time and space scales: 2. Focus on marine low level clouds. Journal of Geophysical Research: Atmospheres, 127, e2021JD035402. https://doi.org/10.1029/2021JD035402, 2022

Houchi, K., Stoffelen, A., Marseille, G. J., & De Kloe, J.: Comparison of wind and wind shear climatologies derived from high-resolution radiosondes and the ECMWF model. *Journal of Geophysical Research: Atmospheres*, *115*(D22), https://doi.org/10.1029/2009JD013196 , 2010

Hourdin, F., Jam, A., Rio, C., Couvreux, F., Sandu, I., Lefebvre, M. P., Brient, F., and Idelkadi, A.: Unified parameterization of convective boundary layer transport and clouds with the thermal plume model. *Journal of Advances in Modeling Earth Systems*, *11*(9), 2910-2933, https://doi.org/10.1029/2019MS001666 , 2019

Houze, R.A.: Mesoscale Convective Systems, Reviews of Geophysics, 42, https://doi.org/10.1029/2004RG000150 , 2004

Iwai, H., Aoki, M., Oshiro, M., and Ishii, S.: Validation of Aeolus Level 2B wind products using wind profilers, ground based Doppler wind lidars, and radiosondes in Japan, Atmos. Meas. Tech., 14, 7255–7275, https://doi.org/10.5194/amt-147255-2021 , 2021.

Jauregui, Y. R., & Chen, S. S.: MJO-induced warm pool eastward extension prior to the onset of El Niño: Observations from 1998 to 2019. *Journal of Climate*, *37*(3), 855-873, https://doi.org/10.1175/JCLI-D-23-0234.1 , 2024

Jensen, E. J., Ueyama, R., Pfister, L., & Atlas, R. L.: The impacts of gravity waves and wind shear on the lifecycle of cirrus clouds in the tropical tropopause layer. *Journal of Geophysical Research: Atmospheres*, *130*(10), e2024JD042308., https://doi.org/10.1029/2024JD042308, 2025

Koning, A. M., Nuijens, L., Mallaun, C., Witschas, B., & Lemmerz, C.: Momentum fluxes from airborne wind measurements in three cumulus cases over land. *Atmospheric Chemistry and Physics, 22*(11), 7373-7388. https://doi.org/10.5194/acp-22-7373-2022 , 2022

Koren I., Oreopoulos, L., Feingold, G., Remer, L.A. and Altaratz, O.: How small is a small cloud?, Atmospheric Chemistry and Physics, 8, 3855–3864, https://doi.org/10.5194/acp-8-3855-2008 , 2008.

Koren, I., Remer, L. A., Altaratz, O., Martins, J. V., & Davidi, A.: Aerosol-induced changes of convective cloud anvils produce strong climate warming. Atmospheric Chemistry and Physics, 10(10), 5001–5010. https://doi.org/10.5194/acp-10-5001-2010 , 2010.

Krisch, I., Hindley, N., Reitebuch, O. and Wright, C.: On the derivation of zonal and meridional wind components from Aeolus horizontal line-of-sight wind, Atmos. Meas. Tech., 15, 3465–3479, 2022 https://doi.org/10.5194/amt-15-3465-2022 , 2022.

Koteswaram, P.: The easterly jet stream in the tropics. *Tellus*, *10*(1), 43-57, https://doi.org/10.3402/tellusa.v10i1.9220 , 1958

Liu, S., Huang, S., Tan, Y., Wen, Z., Chen, X., & Guo, Y.: Characteristics and mechanisms of the interannual variability of the Northwest–Southeast shift of the tropical easterly Jet's core in July. *Journal of Climate*, *37*(11), 3219-3235, https://doi.org/10.1175/JCLI-D-23-0291.1, 2024

Lux, O., Lemmerz, C., Weiler, F., Marksteiner, U., Witschas, B., Rahm, S., Geiß, A., and Reitebuch, O.: Intercomparison of wind observations from the European Space Agency's Aeolus satellite mission and the ALADIN Airborne Demonstrator, Atmos. Meas. Tech., 13, 2075–2097, https://doi.org/10.5194/amt-13-2075-2020 , 2020.

Lux, O., Witschas, B., Geiß, A., Lemmerz, C., Weiler, F., Marksteiner, U., ... and Reitebuch, O.: Quality control and error assessment of the Aeolus L2B wind results from the Joint Aeolus Tropical Atlantic Campaign. *Atmospheric Measurement Techniques Discussions*, *2022*, 1-32, https://doi.org/10.5194/amt-15-6467-2022 , 2022

Marinescu, P. J., Cucurull, L., Apodaca, K., Bucci, L., & Genkova, I.: The characterization and impact of Aeolus wind profile observations in NOAA's regional tropical cyclone model (HWRF). *Quarterly Journal of the Royal Meteorological Society*, *148*(749), 3491-3508, https://doi.org/10.1002/qj.4370 , 2022

Massie, S., Gettelman, A., Randel, W., & Baumgardner, D.: Distribution of tropical cirrus in relation to convection. *Journal of Geophysical Research: Atmospheres*, *107*(D21), AAC-19, https://doi.org/10.1029/2001JD001293 , 2002

McCoy, D. T., Eastman, R., Hartmann, D. L. and Wood, R.: The Change in Low Cloud Cover in a Warmed Climate Inferred from AIRS, MODIS, and ERA-Interim, Journal of Climate, 30, 3609-3620, https://doi.org/10.1175/JCLI-D-15-0734.1 , 2017

McGill, M. J., Yorks, J. E., Scott, V. S., Kupchock, A. W., and Selmer, P. A.: The Cloud-Aerosol Transport System (CATS): a technology demonstration on the International Space Station, Lidar Remote Sensing for Environmental Monitoring XV, edited by: Singh, U. N., International Society for Optics and Photonics, SPIE, 9612, 34–39, https://doi.org/10.1117/12.2190841 , 2015.

Mieslinger, T., Horváth, Á., Buehler, S. A., & Sakradzija, M.: The dependence of shallow cumulus macrophysical properties on large-scale meteorology as observed in ASTER imagery, Journal of Geophysical Research: Atmospheres, 124, 11477–11505. https://doi.org/10.1029/2019JD030768 , 2019.

Mitra, A. P.: Indian ocean experiment [INDOEX]: an overview, 2004, Indian J. Mar. Sci., 33, 30–39, 2004.

Noel, V., Chepfer, H., Chiriaco, M. and Yorks, J.: The diurnal cycle of cloud profiles over land and ocean between 51°S and 51°N, seen by the CATS spaceborne lidar from the International Space Station, Atmospheric Chemistry and Physics, 8, 9457–9473, https://doi.org/10.5194/acp-18-9457-2018 , 2018.

Nuijens, L. and Stevens, B.: The Influence of Wind Speed on Shallow Marine Cumulus Convection, Journal of the Atmospheric Sciences, 69, 168–184, https://doi.org/10.1175/JAS-D-11-02.1 , 2012.

Parker, D. J.: Cold pools in shear, Q. J. Roy. Meteor. Soc., 122, 1655–1674, https://doi.org/10.1002/qj.49712253509 , 1996.

Qu, X., A. Hall, S. Klein, and A. DeAngelis: Positive tropical marine low-cloud cover feedback inferred from cloud-controlling factors. *Geophys. Res. Lett.*, 42, 7767–7775, https://doi.org/10.1002/2015GL065627 , 2015

Reitebuch, O.: The Spaceborne Wind Lidar Mission ADM-Aeolus, in: Atmospheric Physics. Research Topics in Aerospace, edited by: Schumann, U., Springer, Berlin, Heidelberg, https://doi.org/10.1007/978-3-642-30183-4_49 , 2012.

Reitebuch, O., Huber, D., and Nikolaus, I.: Algorithm Theoretical Basis Document ATBD Level1B Products, https://earth.esa.int/eogateway/documents/20142/37627/Aeolus-L1B-Algorithm-ATBD.pdf , 2022

Ratynski, M., Khaykin, S., Hauchecorne, A., Wing, R., Cammas, J.-P., Hello, Y., and Keckhut, P.: Validation of Aeolus wind profiles using ground-based lidar and radiosonde observations at Réunion island and the Observatoire de Haute-Provence, Atmos. Meas. Tech., 16, 997–1016, https://doi.org/10.5194/amt-16-997-2023, 2023.

Rennie, M., Tan, D., Andersson, E., Poli, P., Dabas, A., De Kloe, J., ... and Stoffelen, A.: Aeolus Level-2B algorithm theoretical basis document (mathematical description of the Aeolus Level-2B processor). *Change*, *3*, 23-12, https://earth.esa.int/documents/20142/37627/Aeolus-L2B-Algorithm-ATBD.pdf , 2020

Robe, F. R., and Emanuel, K. A.: The Effect of Vertical Wind Shear on Radiative-Convective Equilibrium States, Journal of the Atmospheric Sciences, 69, 1427–1445, https://doi.org/10.1175/1520-0469(2001)058<1427:TEOVWS>2.0.CO;2, 2001.

Rotunno, R., Klemp, J. B. and Weisman, M. L. - A Theory for Strong, Long-Lived Squall Lines, Journal of the Atmospheric Sciences, 45, 463–485, https://doi.org/10.1175/1520-0469(1988)045<0463:ATFSLL>2.0.CO;2, 1988.

Sassen, K., Wang, Z., & Liu, D.: Cirrus clouds and deep convection in the tropics: Insights from CALIPSO and CloudSat. *Journal of Geophysical Research: Atmospheres*, *114*(D4), https://doi.org/10.1029/2009JD011916, 2009

Sathiyamoorthy, V., Pal, P. K. and Joshi, P. C.: Influence of the Upper-Tropospheric Wind Shear upon Cloud Radiative Forcing in the Asian Monsoon Region, 17, 2725–2735, https://doi.org/10.1175/1520-0442(2004)017<2725:IOTUWS>2.0.CO;2, 2004.

Savazzi, A. C. M., Nuijens, L., Sandu, I., George, G., and Bechtold, P.: The representation of the trade winds in ECMWF forecasts and reanalyses during EUREC^{4}A, Atmos. Chem. Phys., 22, 13049–13066, https://doi.org/10.5194/acp-22-13049-2022 , 2022.

Schulz, B., and Mellado, J. P.: Wind Shear Effects on Radiatively and Evaporatively Driven Stratocumulus Tops, Journal of the Atmospheric Sciences, 75, 3245–3263, https://doi.org/10.1175/JAS-D-18-0027.1, 2018.

Schumacher, R.S., and Rasmussen K.L.: The formation, character and changing nature of mesoscale convective systems, Nature Reviews Earth & Environment, 1, 300-314, https://doi.org/10.1038/s43017-020-0057-7, 2020

Scott, R. C., Myers, T. A., Norris, J. R., Zelinka, M. D., Klein, S. A., Sun, M., & Doelling, D. R.: Observed sensitivity of low-cloud radiative effects to meteorological perturbations over the global oceans. *Journal of Climate*, *33*(18), 7717-7734, https://doi.org/10.1175/JCLI-D-19-1028.1, 2020

Siebesma, P.A., et al.: A Large Eddy Simulation Intercomparison Study of Shallow Cumulus Convection, Journal of the Atmospheric Sciences, 60, 1201-12019, https://doi.org/10.1175/1520-0469(2003)60<1201:ALESIS>2.0.CO;2, 2003

Stoffelen, A., Pailleux, J., Källen, E., Vaughan, M., Isaksen, L., Flamant, P., Wergen, W., Andersson, E., Schyberg, H., Culoma, A., Meynart, R., Endemann, M., and Ingmann, P.: The atmospheric dynamics mission for global wind field measurement, B. Am. Meteorol. Soc., 86, 73–88, https://doi.org/10.1175/BAMS-86-1-73, 2005.

Thorpe, A. J., Miller, M. J., Moncrieff, M. W.: Two-dimensional convection in non-constant shear: A model of mid-latitude squall lines, Q. J. Roy. Meteor. Soc., 108, 739–762, https://doi.org/10.1002/qj.49710845802 , 1982.

Tian, Y., Zhang, Y., Klein, S. A., & Schumacher, C.: Interpreting the diurnal cycle of clouds and precipitation in the ARM GoAmazon observations: Shallow to deep convection transition. *Journal of Geophysical Research: Atmospheres*, *126*(5), e2020JD033766, https://doi.org/10.1029/2020JD033766 , 2021

Voigt, A., Albern, N., Ceppi, P., Grise, K., Li, Y., Medeiros, B.: Clouds, radiation, and atmospheric circulation in the present-day climate and under climate change. WIREs Clim Change. 2021;12:e694. https://doi.org/10.1002/wcc.694, 2021.

Wang, P., Donovan, D. P., van Zadelhoff, G.-J., de Kloe, J., Huber, D., and Reissig, K.: Evaluation of Aeolus feature mask and particle extinction coefficient profile products using CALIPSO data, Atmos. Meas. Tech., 17, 5935–5955, https://doi.org/10.5194/amt-17-5935-2024, 2024.

Wang, S., Golaz, J. C. and Wang, Q.: Effect of intense wind shear across the inversion on stratocumulus clouds, Geophysical Research Letters, 35, L15814, https://doi.org/10.1029/2008GL033865, 2008.

Weiler, F., Kanitz, T., Wernham, D., Rennie, M., Huber, D., Schillinger, M., Saint-Pe, O., Bell, R., Parrinello, T and Reitebuch, O.: Characterization of dark current signal measurements of the ACCDs used on board the Aeolus satellite, Atmos. Meas. Tech., 14, 5153–5177, https://doi.org/10.5194/amt-14-5153-2021, 2021.

Weisman, M. L. Rotunno, R., and Klemp, J. B.: "A Theory for Strong, Long-Lived Squall Lines" revisited, Journal of the Atmospheric Sciences, 55, 361–382, https://doi.org/10.1175/1520-0469(2004)061<0361:ATFSLS>2.0.CO;2, 2004.

1620

Winker, D. M., Hunt, W. H., and Hostetler, C. A.: Status and Performance of the CALIOP Lidar, Proc. SPIE, 5575, 8–15, https://doi.org/10.1117/12.571955, 2004.

Witschas, B., Rahm, S., Dörnbrack, A., Wagner, J., and Rapp, M.: Airborne Wind Lidar Measurements of Vertical and

1625 Horizontal Winds for the Investigation of Orographically Induced Gravity Waves, J. Atmos. Ocean. Technol., 34, 1371–1386, https://doi.org/10.1175/jtech-d-17-0021.1, 2017.

Witschas, B., Lemmerz, C., Geiß, A., Lux, O., Marksteiner, U., Rahm, S., Reitebuch, O., and Weiler, F.: First validation of Aeolus wind observations by airborne Doppler wind lidar measurements, Atmos. Meas. Tech., 13, 2381–2396,

1630 https://doi.org/10.5194/amt-13-2381-2020 , 2020.

Witschas, B., Lemmerz, C., Geiß, A., Lux, O., Marksteiner, U., Rahm, S., Reitebuch, O., Schäfler, A. and Weiler, F.: Validation of the Aeolus L2B wind product with airborne wind lidar measurements in the polar North Atlantic region and in the tropics, Atmos. Meas. Tech., 15, 7049–7070, https://doi.org/10.5194/amt-15-7049-2022 , 2022.

1635

Wood, R.: Stratocumulus clouds, Mon. Weather Rev., 140, 2373–2423, https://doi.org/10.1175/MWR-D-11-00121.1 , 2012.

Zuidema, P.: Convective clouds over the Bay of Bengal. *Monthly Weather Review*, *131*(5), 780-798, https://doi.org/10.1175/1520-0493(2003)131<0780:CCOTBO>2.0.CO;2 , 2003